Understanding the Global Hydrological Droughts of 2003–2016 and their Relationships with Teleconnections

E. Forootan[a,b], M. Khaki[c], M. Schumacher[b], V. Wulfmeyer[b], N. Mehrnegar[a], A.I.J.M. van Dijk[d], L. Brocca[e], S. Farzaneh[f], F. Akinluyi[g], G. Ramillien[h], C.K. Shum[i,j], J. Awange[c], A. Mostafaie[k]

[a]*School of Earth and Ocean Sciences, Cardiff University, United Kingdom*
[b]*Institute of Physics and Meteorology (IPM), University of Hohenheim, Stuttgart, Germany*
[c]*School of Earth and Planetary Sciences, Discipline of Spatial Sciences, Curtin University, Perth, Australia*
[d]*Fenner School of Environment and Society, The Australian National University, Canberra, Australia*
[e]*National Research Council, Research Institute for Geo-Hydrological Protection, Perugia, Italy*
[f]*School of Surveying and Geospatial Engineering, College of Engineering, University of Tehran, Iran*
[g]*Department of Remote Sensing and Geo-science Information System, School of Earth and Mineral Sciences, Federal University of Technology, Akure, Nigeria*
[h]*Centre National de la Recherche Scientifique (CNRS), France*
[i]*Division of Geodetic Science, School of Earth Sciences, Ohio State University, Columbus, Ohio, USA*
[j]*State Key Laboratory of Geodesy and Earth's Dynamics, Institute of Geodesy and Geophysics, Chinese Academy of Sciences, Wuhan 430077, China*
[k]*Surveying Department, Faculty of Engineering, University of Zabol, Iran*

Abstract

Droughts often evolve gradually and cover large areas, and therefore, affect many people and activities. This motivates developing techniques to integrate different satellite observations, to cover large areas, and understand spatial and temporal variability of droughts. In this study, we apply probabilistic techniques to generate satellite derived meteorological, hydrological, and hydro-meteorological drought indices for the world's 156 major river basins covering 2003–2016. The data includes Terrestrial Water Storage (TWS) estimates from the Gravity Recovery And Climate Experiment (GRACE) mission, along with soil moisture, precipitation, and evapotranspiration reanalysis. Different drought characteristics of trends, occurrences, areal-extent, and frequencies corresponding to 3-, 6-, 12-, and 24-month timescales are extracted from these indices. Drought evolution within selected basins of Africa, America, and Asia is interpreted. Canonical Correlation Analysis (CCA) is then applied to find the relationship between global hydro-meteorological droughts and satellite derived Sea Surface Temperature (SST) changes. This relationship is then used to extract regions, where droughts and teleconnections are

Email address: ForootanE@cardiff.ac.uk, ehsforootan@gmail.com (E. Forootan)

strongly interrelated. Our numerical results indicate that the 3- to 6-month hydrological droughts occur more frequently than the other timescales. Longer memory of water storage changes (than water fluxes) has found to be the reason of detecting extended hydrological droughts in regions such as the Middle East and Northern Africa. Through CCA, we show that the El Niño Southern Oscillation (ENSO) has major impact on the magnitude and evolution of hydrological droughts in regions such as the northern parts of Asia and most parts of the Australian continent between 2006 and 2011, as well as droughts in the Amazon basin, South Asia, and North Africa between 2010 and 2012. The Indian ocean Dipole (IOD) and North Atlantic Oscillation (NAO) are found to have regional influence on the evolution of hydrological droughts.

Keywords: GRACE Terrestrial Water Storage (TWS), Global Droughts, Canonical Correlation Analysis (CCA), Sea Surface Temperature (SST), Teleconnections, Drought Hot Spots

1. Introduction

The global hydrological (water) cycle has been under influence of both climate change and anthropogenic modifications (Tiwari et al., 2009; Zhao et al., 2015). A study by Feng and Zhang (2015) suggests that the ongoing global warming could lead to considerable declines in soil water due to a lack of snow melt water recharge to the soil during spring and summer. Increasing the temperature and less water stored in the surface soil moisture might lead to a reduction of precipitation in semi-arid regions. Therefore, the possibility of increasing drought events can be expected in future.

In general, droughts have been categorized into the groups of meteorological or climatological, hydrological, agricultural, and socioeconomic, among which the first two types are of interest in this study (find a critical discussion in Van Loon (2015)). Since drought is a complex phenomenon, there is no universal definition for it (Mishra and Singh, 2010). Often, the term 'meteorological drought' is understood as the shortage in catchment's water fluxes, i.e., precipitation or net precipitation, i.e. precipitation minus evapotranspiration. The term 'hydrological drought' is associated with the shortfalls of water storage, as well as (net) precipitations at the same time. Standardized Precipitation Index (SPI,

McKee et al., 1993; Guttman, 1999) and Standardized Precipitation-Evapotranspiration Index (SPEI, Vicente-Serrano et al., 2010) are often used to represent meteorological droughts. Water storage changes are derived by analyzing soil moisture (and in some cases groundwater) data and used to produce Standardized Soil (Storage) Index (SSI, Mishra and Singh, 2010). In a practical sense, hydro-meteorological droughts may be quantified by relating SPI or $SPEI$ and SSI or by merging variables that are used to define these indices[1] (see e.g., Hao and AghaKouchak, 2013; Carrlão et al., 2016).

Meteorological and hydrological droughts are inter-related through interactions that happen within the water cycle (Van Loon and Laaha, 2015). Generally speaking, any higher than normal net evaporation rates over the oceans can change precipitation rates on land increasing continental water storage (Mueller et al., 2012). In contrast, a shortage in precipitation over land, along with a higher evaporation caused by a meteorological drought may lead to shortage in continental water storage and cause a hydrological drought (e.g., Wilhite, 2000; Tallaksen et al., 2004). Examples of prolonged meteorological drought conditions leading to hydrological droughts are discussed by, e.g., Trigo et al. (2010); van Dijk et al. (2013); Van Loon (2015); Forootan et al. (2017) and Schumacher et al. (2018). Index-based drought monitoring systems are often adopted for operational purpose. Examples include the SPEI (e.g., Beguería et al., 2010) used by the European commission[2] or temperature-precipitation indices by the US's Global Drought Information System[3]. The Global Integrated Drought Monitoring and Prediction System (GIDMaPS) from the University of California Irvine[4] is an experimental system that combines various satellite data and climate re-analysis datasets to compute univariate and multivariate drought indices (see other examples in, e.g., Ahmadalipour et al., 2017). Scientists also base their drought analyses and projections on model simulations, see e.g., Samaniego et al. (2018). A combination of data assimilation and probabilistic forecasting techniques is used in Yan et al. (2017) to generate more realistic seasonal drought forecasts for the USA.

[1] http://spei.csic.es/home.html
[2] http://edo.jrc.ec.europa.eu/gdo/php/index.php?id=2001
[3] www.drought.gov/gdm/
[4] http://drought.eng.uci.edu/

Since the launch of the Gravity Recovery And Climate Experiment (GRACE, Tapley et al., 2004) satellite gravity mission in 2002, drought monitoring studies have been using its estimates of Terrestrial Water Storage (TWS, a vertical integration of surface water, soil moisture, groundwater, and biomass water content) changes to understand global and regional hydrological processes (Chen et al., 2009; Rodell et al., 2009; Frappart et al., 2012; Houborg et al., 2012; Li et al., 2012; Mueller et al., 2012; Long et al., 2013; Thomas et al., 2014; Khaki et al., 2017). For example, Yirdaw et al. (2008) investigated 2002–2003 droughts in the Saskatchewan River basin. In the Murray Darling basin, the hydrological drought of 2002–2006 was found to be related to the meteorological drought that was continued from 2000 (Leblanc et al., 2009; Forootan et al., 2012). Various studies have demonstrated the connection between the long-term trends or changes in the amplitude of seasonal (net) precipitation and TWS (e.g., Zeng, 1999; Seoane et al., 2013; Koster et al., 2000; Strassberg et al., 2007). Khandu et al. (2016); Forootan et al. (2017) and Schumacher et al. (2018), for example, showed that both climate change and anthropogenic contribute to the water storage decline (mainly in groundwater) in South Asia, the Middle East, and Australia, respectively. Other studies indicate that a persistent decrease in seasonal precipitation leads to a decline in TWS (e.g., Voss et al., 2013; Forootan et al., 2014, 2016). Hirschi et al. (2006) studied this effect for 37 mid-latitude river basins in Europe, Asia, North America, and Australia, and drew a similar conclusion. Examples of the application of GRACE data for assessing global water storage trends, seasonal and sub-seasonal variability and extreme events are provided in, e.g., Forootan and Kusche (2012); van Dijk et al. (2014); Eicker et al. (2016); Humphrey et al. (2016); and Kusche et al. (2016).

GRACE has been used to study hydrological droughts (e.g., Houborg et al., 2012; Sinha et al., 2007). For example, Zhao et al. (2017) developed a new monthly global Drought Severity Index (DSI) based on GRACE TWS and showed that it performs comparably to other commonly used drought metrics. In the USA's drought monitoring system[5], GRACE is used for monitoring groundwater droughts. In regional studies,

[5] https://grace.jpl.nasa.gov/applications/drought-monitoring/

Yirdaw et al. (2008) and Awange et al. (2016b) applied the Total Storage Deficit Index (TSDI) proposed by Narasimhan and Srinivasan (2005) using GRACE TWS estimates. Most of these existing studies (e.g., Thomas et al., 2014; Zhao et al., 2015; Awange et al., 2016b; Khandu et al., 2016; Zhang et al., 2016) have applied GRACE TWS to describe the progress of hydrological droughts. It has also been shown that GRACE derived drought indices[6] combining with other satellite products can better characterize droughts (e.g., Australia's Millennium Drought in van Dijk et al., 2013; Zhao et al., 2017, see also). A recent global study by Sun et al. (2017) indicates that GRACE along with satellite derived precipitation data can be used to identify extreme hydrological events, although the study concludes that the length of GRACE data and its low spatial resolution represents a limitation in extracting return periods of extreme events (find a detailed investigation in Kusche et al., 2016).

This study adds to previous research by exploring the relationship between hydro-meteorological droughts and major ocean-atmosphere 'teleconnections'. For this, univariate (i.e., hydrological and meteorological), as well as multivariate (i.e., hydro-meteorological) drought indices are computed for the world's 156 major river basins that are defined by the Global Runoff Data Center[7], and see Figure 1). $SPEI$ and SSI are computed to assess the separate impact of (net) precipitation and water storage changes on the drought evolutions, respectively. We also combine the $SPEI$ and SSI in (a probabilistic way) and develop a Multivariate Standardized Drought Index ($MSDI$) for each basin, which reflect hydro-meteorological drought evolutions (see also Hao and AghaKouchak, 2013; AghaKouchak, 2014; Rajsekhar et al., 2015).

To generate drought indices of this study, long-term precipitation and evapotranspiration data from ERA-Interim (1980–2016, Dee et al., 2011), and TWS from GRACE (2003–2016) are used. We extend the GRACE TWS estimates backwards to 1980 using the water state outputs of W3RA (1980–2012) provided by Schellekens et al. (2017). This extension (i) ensures a better representation of hydrological characteristics of river basins, and (ii) it also mitigates the possible errors in estimating probability density functions

[6] www.ess.uci.edu/~velicogna/drought_data.php
[7] www.fao.org/nr/water/aquastat/irrigationmap/index.stm

that are required to be computed while estimating the desired drought indices. A Monte Carlo approach is applied to estimate the impact of uncertainties of input data and the applied extension backward to 1980 on the estimation of drought indices.

The impact of using GRACE TWS on the estimation of drought indices is compared with alternative indices computed using soil moisture data from ERA-Interim reanalysis. The differences between these indices reflect the contribution of other water compartments (e.g., groundwater and surface water storage) in the evolution of drought indices. Besides, GRACE TWS estimates contain trends, seasonal, and inter-annual variability, which better reflect the impact of climate change and anthropogenic modifications (than land surface models) in the basin scale (also see e.g., Scanlon et al., 2018; Schumacher et al., 2018). Therefore, analyzing GRACE derived drought indices helps us to better understand these interactions.

In order to represent spatio-temporal evolution of droughts, we interpret the computed $SPEI$, SSI, and $MSDI$ of selected basins in the Americas, Africa, Asia, and Australia. Using the computed indices, different drought characteristics such as severity, extent, and frequencies correspond to the 3-, 6-, 12-, and 24- month timescales (suggested by Mpelasoka et al., 2017) are investigated. Canonical Correlation Analysis (CCA, Borga et al., 1998) is applied to relate the computed drought indices with global Sea Surface Temperature (SST, Reynolds et al., 2007) change. This is done for the period of 2003–2016, from which we derive hot spots, where teleconnections appear strongly related to droughts. This investigation, therefore, extends previous efforts that study the relationships between teleconnections and water storage changes (e.g., Garćia-Garćia et al., 2011; Philips et al., 2012; Anyah et al., 2018; Eicker et al., 2016; Forootan et al., 2018; Ni et al., 2018).

In summary, this study has three major contributions: (A) it provides new insights about global scale drought evolution while focusing on the values water storage estimations derived from GRACE, (B) it evaluates and discusses the properties of global hydrological droughts during 2003–2016 and their uncertainties, and finally (C) it explores relationships between ocean-atmosphere teleconnections and hydro-meteorological droughts over multiple regions.

FIGURE 1

2. Data

2.1. Terrestrial Water Storage Estimates from GRACE

GRACE Level 2 (L2) products consist of monthly gravity field solutions. The latest release of L2 data (RL06) covering January 2003 to December 2015 truncated at spherical harmonic degree and order 90 are downloaded from the Center for Space Research (CSR)[8]. These residual coefficients represent mainly water mass changes on continents (Ramillien et al., 2005). Degree 1 coefficients are replaced with those estimated by Swenson et al. (2008) to account for the movement of the Earth's center of mass. Degree 2 and order 0 coefficients are replaced by those from Satellite Laser Ranging (SLR), which are more stable than those of GRACE (e.g., Chen et al., 2007). Anomalies due to the Glacial Isostatic Adjustment (GIA) are reduced using the output of the model provided by Geruo et al. (2013). Correlated noise in L2 products is reduced by applying the DDK2 anisotropic filter (Kusche et al., 2009). The smoothed fields are then converted to TWS changes following Wahr et al. (1998). Basin average values for the 156 river basins of Figure 1 and their errors are estimated following (e.g., Khaki et al., 2018a). Our computations cover the complete mission period of 2003–2016, where Figure 2 shows the standard deviations of basin averaged GRACE TWS, their errors, and the signal to noise ratio within each basin of Figure 1. During 2003–2016, the computed basin averaged time series are temporally interpolated (using a harmonic interpolation). This is also applied to other data sets, thus, all available data records have been synchronized. Besides, since other data sets have a spatial resolution different than that of GRACE L2 data, they are converted to the spectral domain and truncated at spherical harmonic degree and order 90 and basin averages are computed following Khaki et al. (2018a).

FIGURE 2

[8] http://www2.csr.utexas.edu/grace/

2.2. Global Soil Moisture, Precipitation, and Evapotranspiration Products

ERA-Interim is a global atmospheric reanalysis produced by the European Center for Medium Range Weather Forecast (ECMWF, Dee et al., 2011). The reanalysis delivers several key land surface parameters such as soil moisture, vegetation, and snow, among others by combining various global observational datasets using an integrated forecast model. In this study, monthly soil moisture data from four volumetric layers are obtained from 6 hourly $0.25^\circ \times 0.25^\circ$ soil moisture data[9]. To account for meteorological changes, global precipitation and evapotranspiration data are used from the provided link and the vertical layers are summed up.

The ERA-Interim data, used in this study, cover the period of 1980–2016. Possible lateral water storage flow has not been explicitly considered in the ERA-Interim's soil moisture simulations, which might affect drought indices derived from soil moisture by incorporating higher/lower flow in some cases such as winter and after snow melt. To mitigate the inconsistencies between the above data, and improve the accuracy of water storage and water flux estimations, all above data (GRACE TWS, ERA-Interim's soil moisture, precipitation, and evapotranspiration) are spatially averaged within the 156 river basins of Figure 1. It is worth mentioning that the rate of change in TWS is related to the net precipitation through the water balance equation. However, it has been shown that GRACE TWS contains long memory of hydrological processes, while fluxes such as precipitation and evapotranspiration introduce water variation with shorter wavelength (e.g., Rakovec et al., 2016; Forootan et al., 2017). Therefore, combining GRACE TWS and net precipitation data (see Section 3.2) seems to be suitable to explore hydro-meteorological drought characteristics (see, e.g., Sun et al., 2017).

2.3. Sea Surface Temperature Data

The Version 2 of the daily Optimum Interpolation Sea Surface Temperature (OISST) data with $0.25^\circ \times 0.25^\circ$ spatial resolution between 2002 and 2016 are used. Infrared satellite data from the Advanced Very High Resolution Radiometer (AVHRR), in situ observations (International Comprehensive Ocean Atmosphere Dataset, Worley et al., 2005),

[9] http://apps.ecmwf.int/datasets/data/interim-full-daily/

and proxies computed from sea ice concentrations are used to generate the OISST v2 (Reynolds et al., 2007).

TABLE 1

3. Method

3.1. Extending GRACE TWS Time Series Backwards to 1980

Extreme events, such as droughts, are often characterized by their duration, magnitude (or intensity), extent, and return period. A reliable estimation of these characteristics requires time series that are long enough and are also well representative of hydro-meteorological characteristics of the regions of interest (Cancelliere and Salas , 2004). However, a limitation of GRACE data in drought monitoring applications is the mission's limited operational time, i.e. 2002–2017. To mitigate this problem, we use TWS simulation of ten global models that are published by Schellekens et al. (2017) covering 1979–2012. From these, the W3RA model (van Dijk., 2010) is applied to extend GRACE TWS in the 156 river basins of Figure 1, and TWS of other nine models is used to estimate uncertainties using the collocation approach of Awange et al. (2016a). It is worth mentioning that using simulated TWS data, even after applying the following corrections, is not a perfect choice and the estimated drought indices might be still over-/under-estimated. However, this impact if far smaller than using short length data sets to compute drought indices.

To extend the TWS estimates backward to 1980, a scale factor and a bias (vertical shift) are estimated to match the long-term W3RA TWS to that of GRACE as

$$X_{W3RA} = a^{-1} * X_{GRACE} - b, \tag{1}$$

using the common data of 2003–2013. This means that following Scanlon et al. (2018)'s conclusion, the basin-averaged GRACE derived TWS estimates are assumed to be more realistic than model simulations, in terms of trends, as well as seasonal and inter-annual variations. Therefore, in Eq. (1), we consider $a * X_{W3RA}$ for the period of 1980–2013

and extend GRACE data backward. In is worth mentioning that here the bias between W3RA and GRACE is assumed to be temporally invariant, which is not a sophisticated assumption. Applying a time-variable bias correction, however, requires a careful extra research and is out of scope of this study. Errors of the extension in Eq. (1) is computed using a least squares error propagation Koch (1998), while considering the error fields of Figure 2 (Middle). Examples of the original W3RA TWS and the extended time series in the Ganges and Nile River basins are shown in Figure 3. The extended TWS time series of 1980–2016 are used to compute hydrological indices as described in what follows.

FIGURE 3

3.2. Multivariate Standardized Drought Index

Three different drought indices of Standardized Precipitation-Evapotranspiration Index ($SPEI$), Standardized Soil moisture (Storage) Index (SSI), and Multivariate Standardized Drought Index ($MSDI$) are estimated to represent different types of droughts. $SPEI$ is computed similar to Vicente-Serrano et al. (2010), which is similar to the SPI in McKee et al. (1993). In this approach, wet or dry condition are estimated based on the frequency distribution of variables (here net precipitations) on a variety of timescales from sub-seasonal to inter-annual scales. To compute $SPEI$, we first fit a gamma probability density function to the observed net precipitation (1980–2013) and compute their cumulative distribution. Then, these are transformed to standard normal distributions following (Wu et al., 2001). The transformed probability varies between +3.0 and -3.0 (Edwards et al., 1997), which indicates the level of wetness and dryness, respectively. In this study, SSIs are computed similar to $SPEI$s, but soil moisture data from ERA-Interim or GRACE TWS estimates are used as inputs.

Generating $MSDI$ follows a statistical approach that allows us to simultaneously incorporate the information of $SPEI$ and SSI. Thus, the temporal averaging of the three drought indices used in this study is treated consistently. For each two types of samples (X and Y), the cumulative joint probability density function (Pr) is expressed

as

$$Pr(X \leq x, Y \leq y) = C(F(X), F(Y)) = q, \tag{2}$$

where C is a copula, and $F(X)$ and $F(Y)$ are the marginal cumulative distribution functions, and finally q is the cumulative joint probability value (Hao and AghaKouchak, 2013). In Eq. (2), time series of net precipitation and soil moisture or TWS changes can replace the random variables of X and Y. We use Frank copula to model the joint distribution in Eq. (2). Following Hao and AghaKouchak (2013), $MSDI$ can be computed as

$$M = \Phi^{-1}(q), \tag{3}$$

where Φ is the standard normal distribution function, which is computed here empirically. In all the above drought indices, the negative index represents that the climate condition is dry (drought), while a positive index indicates a wet climate condition (AghaKouchak, 2014).

Uncertainty of the Computed Drought Indices:

To account for the uncertainty of input data, while estimating drought indices, a Monte Carlo approach is implemented. For this, we generate samples of soil moisture, TWS, and net precipitation data from a random distribution $\mathbf{N}(\mu, \sigma)$, where μ represents the mean values derived by processing the input data in Section 2, and σ of TWS and soil moisture is derived from the results of Figure 2 (Middle). For basin averaged net precipitation, we consider a multiplicative error of 30% (Tian et al., 2013). To estimate the uncertainty of drought indices, we generate 1000 samples of TWS and net precipitation time series. As a result, 1000 sets of respective drought indices are computed, whose median and range are used to interpret the severity of droughts and their uncertainties, respectively.

Types of Drought Indices Estimated in this Study:

As mentioned, for each river basin of Figure 1, the $SPEI$ is calculated using net precipitation from ERA-Interim data, while SSI_{Sm} is based on ERA-Interim's soil moisture data that largely represent agricultural droughts, and SSI_{TWS} is computed using GRACE TWS data. In a probabilistic manner (Eq. (3)), $MSDI_{Sm}$ is estimated by simultaneously using ERA-Interim soil moisture and net precipitation from ERA-Interim. Finally, $MSDI_{TWS}$ is derived by combining GRACE TWS and net precipitation data from ERA-Interim. Therefore, our estimate $MSDIs$ will likely represent hydro-meteorological droughts.

3.3. Extracting Drought Characteristics in Different Timescales

To better analyze drought characteristics using the various drought indices, different timescales are considered. Averaging periods of 3-, 6-, 12- and 24-month are used here to extract persistent patterns. These timescales are generally relevant to a range of agricultural and hydrological systems and facilitate a better interpretation of drought events (Mpelasoka et al., 2017). For any of these timescales, a drought event begins when the drought indices are continuously less than -0.9 for at least 3 months (dry condition threshold suggested by Mpelasoka et al., 2017).

3.4. Canonical Correlation Analysis (CCA)

CCA seeks to find the linear relationship between two sets of multidimensional variables x and y. CCA extracts canonical coefficients u and v such that $X = x^T u$ and $Y = y^T v$ (X and Y are canonical variates) possess a maximum correlation coefficient (Chang et al., 2013) using the following function,

$$\begin{aligned} R &= \frac{E[XY]}{sqrt(E[X^2]E[Y^2])} \\ &= \frac{E[u^T x y^T v]}{sqrt(E[u^T x x^T u]E[v^T y y^T v])} \\ &= \frac{u^T C_{xy} v}{sqrt(u^T C_{xx} u v^T C_{yy} v])}, \end{aligned} \tag{4}$$

where C_{xx} and C_{yy} are covariance matrices of x and y, respectively and the objective in above function is to maximize the correlation R. We use an eigenvalue decomposition procedure (Forootan, 2014) to find the linear weights producing canonical coefficients, which imply maximum possible correlations (see details in Steiger and Browne, 1984). There are different canonical coefficients within each set (at most minimum of variable numbers in X and Y) leading to different uncorrelated coefficients. Nevertheless, the combination of variables with the first canonical coefficient for each set has the highest possible multiple correlations with the variables in the other set.

Once the coefficients are calculated, they can be used to find the projection of x and y onto u and v as canonical variates with maximum correlations. In this study, x contains the vectors of $SPEI$, SSI, and $MSDI$ time series calculated for the 156 river basins of Figure 1, while y contains SST data. Different grid windows ($5°\times5°$) are selected over the oceans including regions, where El Niño Southern Oscillation (ENSO; Barnston et al., 1987), North Atlantic Oscillation (NAO; Barnston et al., 1987), and Indian Ocean Dipole (IOD; Rao et al., 2002), as well as regions randomly selected in other oceanic basins as shown in Figure 4. These choices can help to better capture the global climate impact on the land hydrological events. SST data over different boxes (cf. Figure 4) are preferred over the climate indicators (e.g., ENSO, IOD, and NAO indices, see Table 1 for their corresponding references) because: (1) larger number of input variables in the CCA can improve its performance to extract the optimize relationship between predictors (i.e., SST or teleconnection indices) and predictands (i.e., drought indices), (2) spatially distributed boxes better represent oceanic variations than single indices, and (3) SST is a better predictor of precipitation than pressure anomaly often used to produce climate indices (e.g., L'Heureux et al., 2015). These facts will likely result in better predictions of global droughts.

FIGURE 4

4. Results

4.1. Drought Indices

Here, we first summarize the global drought results derived by computing $SPEI$, SSI, and $MSDI$ for the 156 basins (locations are depicted in Figure 1). The annual average of each drought index including SPEI, SSI (SSI_{Sm} and SSI_{TWS}), and MSDI ($MSDI_{Sm}$ and $MSDI_{TWS}$) are calculated for the period of 2004 to 2016. Figure 5 shows an example of the averaged drought indices computed in 2008. Maps of other years can be found in the Electronic Supplementary Material (ESM).

FIGURE 5

In general, several similarities are found between $SPEI$, SSI_{Sm} by ERA-Interim, and SSI_{TWS} by GRACE, e.g., for basins located in the Australian continent or North America. These indices, however, contain considerable differences in terms of amplitude and phase. For example, it can be seen that there are stronger agreements between SSI_{SM} or $MSDI_{Sm}$ and $SPEI$ than between SSI_{TWS} or $MSDI_{TWS}$ and $SPEI$. The reason is that changes in soil moisture has a higher correlation with net precipitation than GRACE TWS. Because, in general, changes in TWS involve complicated surface and sub-surface processes, while soil moisture changes is dominated by precipitation variations (see, e.g., Brocca et al., 2013). We also find that in some basins $MSDI$ fits better to SSI indices than $SPEI$ such as those located in the north part of Africa. This similarity indicates that water storage deficiency is likely the dominant contribution in hydrological drought evolution within these basins.

Correlations between different pairs of drought indices (2003–2016) are shown in Figure 6. Overall, the SSI from both GRACE TWS and ERA-Interim's soil moisture (SSI_{Sm} or SSI_{TWS}) indicates more pronounced dry and wet episodes than $SPEI$ and $MSDI$. The reason is that $SPEI$ and $MSDI$ incorporate net precipitation, which contains higher frequency oscillations than the water storage records used in the SSI (SSI_{Sm} or SSI_{TWS}). Stronger multi-year trends in water storage data leads to hydrological drought indices with higher magnitude.

FIGURE 6

Figure 7 presents average trends of $SPEI$, SSI_{TWS} and $MSDI_{TWS}$ (derived from GRACE) for the 156 basins during the study period (2004–2016). It can be seen that the $MSDI$ over some regions such as the Nile basin and South America is closer to $SPEI$, and in some other cases is closer to SSI, e.g., within Asia and the Australia's western parts. In the Nile basin, climate variability plays the major role, e.g., through precipitation (Awange et al., 2014; Omondi et al., 2014), which is better reflected in the estimated $SPEI$ and $MSDI$. On the other hand, in the case of Asia and specifically Middle East, water storage changes, mainly due to anthropogenic impacts, largely drive the evolution of drought indices, especially those of GRACE TWS (also shown in Figure 6). This impact can be seen in SSI_{TWS} and $MSDI_{TWS}$. Most of the basins located in Middle East exhibit long-term droughts caused by persistent below normal precipitation and decline in water storage (see e.g., Forootan et al., 2017; Khaki et al., 2018b). In the southern parts of South America, the negative trend can be related to the ice loss over e.g., the Patagonian Ice Fields (e.g., Foresta et al., 2018). Minor effects can also be caused by the 2010 Maule earthquake. On the other hand, some parts such as the southeast and northeast parts of Asia experience a positive precipitation trend. As a result, $SPEI$ indicates wet episodes in these regions. Negative values seen in the $SPEI$ over the Nile basin are also reflected in the $MSDI$ even though water storage remains in the normal range, thus, shows that less than normal net precipitation causes droughts in this basin.

FIGURE 7

Here, we select 12 basins (of various hydro-climatological conditions) to discuss the characteristics of drought indices. These include the Mississippi and Colorado basins from North America, the Amazon and Salado Atlantico basins from South America, as well as the Ganges, Brahmaputra, and Euphrates basins from Asia, and finally the Niger, Chad, Nile and Congo basins in Africa. To this end, for any of these basins, spatially

averaged $SPEI$, SSI (both from ERA-Interim and GRACE), and $MSDI$ (derived from ERA-Interim and GRACE) during the study period are computed and demonstrated in Figures 8 and 9. To enhance the visual comparisons, errors of the drought indices are not shown in these figures.

We find similarities between all the drought indices within the Nile (except during 2014–2016) and Amazon basins, which show that net precipitation and water storage changes are highly correlated in these basins. The important difference between $SPEI$ and SSI or $MSDI$ are found to be a phase shift of 1 to 6 months. The values of SSI and $MSDI$ change slower than $SPEI$ from one year to other. This, for example, describes the main differences between $SPEI$ and $MSDI$ or SSI in the Nile basin, where the net precipitation decrease, e.g., in 2008 (due to La Niña) and the deficiency of incoming water slowly changes the SSI of 2008–2010 (compare the green and black curves in Figure 8-Nile).

In general, our estimated $SPEI$s are found to be often different from the SSIs and $MSDI$s in other basins. Over the Euphrates (cf. Figure 9), $SPEI$ shows a wet period in 2011 and 2013 ($SPEI > 1$, indicating wet and very wet episodes), while other indices represent dry periods (starting in 2008 and the SSI values changes from 0 to less than -2 in 2015). A similar pattern can be seen in Ganges, Brahmaputra, and Euphrates. This is due to a long-term water storage depletion in these basins (see Figure 7), even though $SPEI$ and SSI_{Sm} often shows positive values (e.g., during 2013–2014 in the Ganges).

In addition to the phase shifts between $SPEI$ and other SSI or $MSDI$, remarkable amplitude discrepancies are also found within most of the basins, e.g., Lake Chad 2007–2009, Mississippi 2010–2012, and Colorado 2013–2016 (Figure 8). The reason is mainly attributed to the multi-year trend in the water storage changes, which requires a long period of wet or dry episodes to return to a normal level.

FIGURE 8

FIGURE 9

In summary, the results indicate that the realistic water storage oscillations and trends

in GRACE TWS data considerably change the magnitude and timing of drought indices in the assessed basins. However, using only GRACE data to assess hydrological drought will be likely misleading, since the SSI and $MSDI$ indices can be dominantly influenced by existing TWS trends, which is evident by comparing the green and cyan curves in Figure 9. This will be clearer if one compares the indices time series with water storage variations. Thus, average groundwater and soil moisture time series are obtained from the WaterGAP Global Hydrology Model (WGHM; more details on Döll et al., 2003; Müller et al., 2014) within four selected basins, i.e., Ganges, Brahmaputra, Euphrates, and South interior. WGHM is chosen here because, beside accounting for the dominant hydrological processes that occur on the spatial scale of 50 km, it also accounts for human water use. However, it should be noted that WGHM's simulations contain uncertainties, thus, its outputs might be interpreted with caution. The comparison performed here is to assess hydrological droughts from an independent source rather than GRACE TWS estimates. From our results, it can be seen that negative groundwater trends are largely captured by SSI_{TWS} and to a lesser degree by $MSDI_{TWS}$. Moreover, the differences between soil moisture and groundwater variations can explain the large discrepancies between SSI_{Sm} and SSI_{TWS}. This discrepancy, however, does not equally impact $MSDI$. These result confirm our previous finding that the estimated SSI indices are more sensitive to water storage changes than $MSDI$.

In Figure 10, we demonstrate the impact of uncertainties on the phase and magnitude of the drought indices for the two basins of Amazon and Ganges. Our numerical results indicate that considering 30% multiplicative errors result in up to 1-level in the magnitude of $SPEI$s. For computing SSIs, while considering the realistic errors of Figure 2 (Middle), an error of up to 0.7-level is estimated for the magnitude of SSIs. As a result, the uncertainty of MSDIs is dominated by the error of net precipitation as can be seen in Figure 10. These uncertainties cause an error in estimating the timing of droughts with certain level of severity, which can reach up to 3 to 6 months. It is also worth mentioning that the magnitude of the estimated drought indices, discussed above, depends on the model data used to extend GRACE TWS backward to 1980. However, our numerical assessments (not shown here) indicate that the choice of model has only marginally effect,

433 which is less than the level of uncertainty shown in Figure 10.

FIGURE 10

434 *4.2. Characteristics of Global Droughts*

435 In this section, we analyze drought and its spatial and temporal variations within the
436 156 river basins of this study. To this end, following Mpelasoka et al. (2017), drought
437 indices are considered at four timescales of 3-, 6-, 12- and 24-month. For any of these
438 timescales, the drought indices are calculated and are assumed to be a drought when
439 they are continuously less than -0.9 for at least three months (dry condition threshold
440 suggested by Mpelasoka et al., 2017). Figure 11 illustrates the frequency (month per
441 year) of detected droughts for each timescale by $SPEI$, SSI and $MSDI$ derived from
442 GRACE. This figure shows the major drought timescale is 3-month suggested by all
443 indices. It can be found from this figure that the longer timescale is considered, the
444 less likely a drought may occur. As an instance, for 24-month timescale, droughts are
445 detected for only few regions (e.g., in the Middle East and Africa). We also find that
446 drought with longer timescales, e.g., 12-month droughts, can be detected from SSI in
447 regions such as the Middle East and Northern Africa, while this cannot be detected using
448 $SPEI$ (compare Figure 11 top-right with middle-right). This is mainly attributed to the
449 longer memory of TWS (than net precipitation), which has led to extended hydrological
450 droughts in these regions. One can also see that the SSIs derived from GRACE are
451 stronger than the $SPEI$s, showing that hydrological processes (and their trends) must
452 be considered in analyzing drought patterns, e.g., for monitoring agricultural droughts.
453 More frequent drought conditions are captured by the indices within Middle East, North
454 America, and North West parts of Asia.

FIGURE 11

455 We further investigate the spatial variations of drought over each basins by measuring
456 the portion of grid points exhibiting droughts (for any timescale) to the number of grid
457 points in each basin. This is done for the period of 2002 to 2016, from which time series of

the drought area extent for 12 basins are plotted in Figures 12 and 13. From these results, the estimates of SSI and $MSDI$ that use GRACE data are closer compared to $SPEI$. Larger areas can be found with drought conditions during 2003 and 2004 in the Ganges, Niger, and Brahmaputra basins, 2014–2016 in the Colorado Euphrates, and South interior mainly from the SSI and $MSDI$ calculations. A considerable drought extent can be observed for the Congo basin between 2006 and 2008. During 2012, considerable spatially extended droughts are found in the Salado Atlantico, Niger, Nile+Red Sea neighbor, and Congo basins. In the Colorado basin, while GRACE derived $SPEI$ does not show any major drought, both SSI and $MSDI$ depict a strong anomaly, which can be explained by limited rainfalls.

FIGURE 12

FIGURE 13

We also calculate time series that reflect the evolution of the percentage of area in each basin affected by different types of droughts. Linear trends are computed for these spatial extents and are displayed in Figure 14. In this figure, drought trends of area extent are estimated for different timescales of 3-, 6- and 12-month, using $SPEI$, SSI from GRACE, and $MSDI$ derived from GRACE data and net precipitation (P-E). The results indicate that the estimated trends are positive in most of the basins, for example, in the Middle East and the southern parts of Africa. Confirming the previous results, Figure 14 indicates that the application of GRACE data in computing SSI and $MSDI$ reveal stronger drought patterns, which are distributed over larger areas. To complement our investigation, we investigate the extent of droughts in the Niger (Ferreira et al., 2018), Ganges and Brahmaputra (Khandu et al., 2016), Mississippi (Folger and Cody, 2015), Danube (ICPDR, 2017), and Zambezi (Siderius et al., 2018) as investigated in previous studies. The results of area extent covered by the three drought indices are reported in Table 2, which indicate that precipitation deficit in the Niger and Danube basins and water storage deficit in other basins are the main drivers of droughts in these regions.

FIGURE 14

4.3. CCA Results to Explore Drought and Teleconnection Hot-spots

In this section, CCA is applied to relate drought indices ($SPEI$, SSI, and $MSDI$ from GRACE and net precipitation) within the 156 basins of Figure 1 and the SST average in 31 windows ($5°\times5°$) distributed over the oceans (Figure 4). In order to achieve the best results, these windows are located in places where stronger correlation coefficients between SST and the ENSO, NAO, and IOD indices can be found. At each grid point, CCA establishes the connection between SST values of all windows on the one hand and drought indices on the other hand. This connection appears as a set of weight values for each SST window and each drought index. Therefore, after applying CCA, combinations of drought indices are achieved at each grid point in a way that each drought index is being assigned a different weight. The average of computed weights for $SPEI$, SSI and $MSDI$ are found to be 18%, 42%, and 40%, respectively. This shows that SSI and $MSDI$ are well related to SST data and has the largest impact in the drought combinations, which can be related to the both effects of rainfall and shortage in water storage (derived from GRACE data) in drought evolutions. The average extracted combinations of the drought indices in 12 selected basins of Figures 12 and 13 are shown in Figures 15 and 16.

FIGURE 15

FIGURE 16

From Figures 15 and 16, multiple droughts are found within the 12 selected basins, e.g., during 2012 over Mississippi and Colorado, 2012 over Salado Atlantico, Amazon, and Euphrates, 2008 over Euphrates, South interior, and Mississippi. Despite some similarities, some of these patterns have not been captured by individual indices. Besides, CCA guarantees that the extracted droughts better describe SST variations related to ocean-atmosphere phenomena including ENSO, IOD, and NAO. We compare the performance of the extracted drought by CCA to $SPEI$, SSI, and $MSDI$. Considering the 31 boxes in Figure 4, the estimated correlation coefficients between the drought indices and

509 the grid cell located in the ENSO, NAO, and IOD area are found to be higher than other
510 SST time series showing their dominant impact on net precipitation and TWS changes
511 (see the results in Table 3). Detailed correlation maps (between each drought index and
512 all the climate indicators) can be found in the Supplementary Material.

513 Considering the values of the correlation coefficients in Table 3, a stronger relation-
514 ship is found between hydrological droughts and ENSO (maximum correlation coefficient
515 of 0.75 between MSDI and ENSO). Correlation coefficients of drought indices and other
516 climate indicators such as NAO and IOD are found to be moderate. A maximum corre-
517 lation coefficient of 0.67 (on average) is found between $MSDI$ and ENSO, which shows
518 stronger agreement between indices and ENSO. These results indicate that ENSO is a
519 dominant climate mode with widespread influence, whereas IOD and NAO have more
520 localized influence (see, e.g., van Dijk et al., 2013; Anyah et al., 2018).

TABLE 3

521 In Figure 17, annually averaged drought indices predicted by CCA are shown for the
522 156 basins (cf. Figure 1) covering 2004–2015. Negative values of [-3 -1] indicate strong
523 relationships between SST changes and the evolution of droughts. The results indicate
524 that central to northern parts of Asia exhibit a drought condition in most of the years
525 shown in Figure 17. Most parts of Australian continent experience droughts between
526 2006 and 2011. Similar drought conditions are also found to be dominant within the
527 north part of America, especially in the Mississippi basin during 2004 to 2007. The 2005
528 drought over the Amazon basin is captured by the CCA results. During 2003–2012, the
529 eastern parts of Africa (e.g., Nile basin) towards its southern parts are found to be dry,
530 in particular, in 2007, 2011, 2012, and 2014.

FIGURE 17

5. Conclusion

Large scale drought events, which strongly influence global and regional water resources, can be determined using hydro-climate variables. In this study, traditional univariate, as well as probabilistic multivariate drought indices are estimated by combining monthly Terrestrial Water Storage (TWS) change data from GRACE, as well as ERA-Interim's soil moisture, precipitation, and evapotranspiration products. These indices are estimated for the worlds' 156 major river basins covering 2002–2016, and they reflect both hydrological and meteorological evolutions within these basins. Different drought characteristics of trends, occurrences, areal extent, and frequencies for the 3-, 6-, 12-, and 24-month timescales are computed using these indices. We also applied Canonical Correlation Analysis (CCA) to understand relationships between the spatial and temporal evolution of the estimated hydrological droughts and the major large-scale ocean-atmosphere interactions. In summary, we conclude that:

- The 3-month and 6-month drought timescale are found to be repeated more frequently (than those of longer timescales), globally.

- In most of the basins, we observe an increase in magnitude, extent, and in some cases, length of hydrological droughts, which could be due to, e.g., less precipitation and more evapotranspiration beside excessive water usage.

- The Multivariate Standardized Drought Indices ($MSDI$) derived by combining GRACE Terrestrial Water Storage (TWS) and net precipitation, as well as ERA-Interim soil moisture and net precipitation are found to be better correlated to global Sea Surface Temperature (SST) data compared to those drought indices derived only from water storage data (Standardized Soil moisture (Storage) Index, SSI) or from net precipitation (Standardized Precipitation Index, $SPEI$). Besides, the combination of drought indices of $SPEI$, SSI, and $MSDI$ estimated by CCA indicates a strong connection to the major large-scale ocean-atmosphere phenomena (e.g., El Niño Southern Oscillation, North Atlantic Ocean, and Indian Ocean Dipole). Therefore, CCA might be a useful approach to predict global droughts,

559 while knowing the predicted state of SST or the ENSO and other teleconnection
560 indices.

561 • GRACE TWS data contain multi-year variations and trend, which are not well
562 presented in hydrological model simulations and re-analysis data. Therefore, using
563 GRACE data in producing SSI and $MSDI$ better reflects hydro-climatological
564 characteristics of global river basins. However, one needs to be aware of unwanted
565 anomalies in GRACE fields such as those related to the surface deformation and
566 those due to earthquakes. A possible way to eliminate this problem can be achieved
567 through a careful assimilation of GRACE data into hydrological models, (e.g.,
568 Khaki et al., 2018b; Schumacher et al., 2018), which will be addressed in future
569 studies.

570 • Uncertainty in input data can cause an error in estimation of the severity of droughts
571 and also introduces a phase shift. Basin-averaged drought indices derived from
572 GRACE TWS are found to be generally more certain than those estimated using
573 ERA-Interim data with a multiplicative error of 30%

574 • CCA results reveal regional patterns of hydrological droughts, e.g., the northern
575 parts of Asia and most parts of Australian continent between 2006 and 2011, which
576 are found to be strongly correlated with the ENSO and the Indian Ocean Dipole
577 (IOD) climate variabilities. Correlation coefficients between drought indices and
578 the North Atlantic Oscillation are found to be moderate.

579 Overall, we conclude that the application of CCA on different hydrological indices (de-
580 rived by combining data from different satellite missions) and SST data permits the
581 identification of regions where the interactions between hydrological droughts and tele-
582 connection are strong. This is investigated here for the period of 2003–2016. In the
583 future, this type of analysis by hydrological indices would be completed with new and
584 updated satellite data, in particular the ones provided by the geodetic mission GRACE
585 Follow-On launched in 2018.

Acknowledgments

Authors thank the editor Prof. Ralf Ludwig and two anonymous reviewers for their valuable comments, which we used to improve this study. We are also grateful to the data used in this study that are freely available from their providers.

References

AghaKouchak, A. (2014); A baseline probabilistic drought forecasting framework using standardized soil moisture index: application to the 2012 United States drought. Hydrol. Earth Syst. Sci., 18, 2485-2492, doi:10.5194/hess-18-2485-2014.

Ahmadalipour A., Moradkhani H., Yan H., Zarekarizi M. (2017); Remote sensing of drought: vegetation, soil moisture, and data assimilation. In: Lakshmi V. (eds) Remote Sensing of Hydrological Extremes. Springer Remote Sensing/Photogrammetry. Springer, Cham, doi:10.1007/978-3-319-43744-6_7

Anyah, R.O., Forootan, E., Awange, J.L., Khaki, M. (2018); Understanding linkages between global climate indices and terrestrial water storage changes over Africa using GRACE products. Science of The Total Environment, 635, 1405-1416, doi:10.1016/j.scitotenv.2018.04.159.

Awange, J.L., Forootan, E., Kuhn, M., Kusche, J., Heck, B. (2014); Water storage changes and climate variability within the Nile basin between 2002 and 2011. Advances in Water Resources, 73, 1-15, doi:10.1016/j.advwatres.2014.06.010.

Awange, J. , Ferreira, V. , Forootan, E. , Khandu, , AndamAkorful, S. , Agutu, N. He, X. (2016a); Uncertainties in remotely sensed precipitation data over Africa. International Journal of Climatology, 36, 303–323. doi:10.1002/joc.4346.

Awange, J.L., Khandu, Schumacher, M., Forootan, E., Heck, B. (2016b); Exploring hydro-meteorological drought patterns over the Greater Horn of Africa (1979–2014) using remote sensing and reanalysis products. Advances in Water Resources, 94, 45-59, doi:10.1016/j.advwatres.2016.04.005.

612 Barnston, A.G., Livezey, R.E. (1987); Classification, seasonality, and persistence of low-
613 frequency atmospheric circulation patterns. Mon. Weather Rev. 115, 1083-1126.

614 Barnston, A.G., Tippett, M.K., Shuhua, L. (2012); Performance of Recent Multimodel
615 ENSO Forecasts. J. Appl. Meteor. Climatol., 51, 637-654, doi:10.1175/JAMC-D-11-
616 093.1.

617 Beguería, S., Vicente-Serrano, S.M., Angulo, M., (2010); A multi-scalar global drought
618 dataset: the SPEIbase: A new gridded product for the analysis of drought vari-
619 ability and impacts. Bulletin of the American Meteorological Society, 91, 1351-1354,
620 doi:10.1175/2010BAMS2988.1.

621 Borga, M. (1998); Learning multidimensional signal processing. PhD thesis, Linkoping
622 University, Sweden, SE-581 83 Linkoping, Sweden. Dissertation No 531, ISBN 91-7219-
623 202-X, http://people.imt.liu.se/magnus/.

624 Brocca, L., Moramarco, T., Melone, F., Wagner, W. (2013); A new method for rainfall
625 estimation through soil moisture observations, Geophys. Res. Lett., 40, 853-858, doi:
626 10.1002/grl.50173.

627 Cancelliere, A., and J. D. Salas (2004); Drought length properties for periodicstochastic
628 hydrologic data, Water Resour. Res., 40, W02503, doi: 10.1029/2002WR001750.

629 Carrlão, H., Russo, S., Sepulcre-Canto, G., Barbosa, P. (2016); An empirical standardized
630 soil moisture index for agricultural drought assessment from remotely sensed data.
631 International Journal of Applied Earth Observation and Geoinformation, 48, 74-84,
632 doi:10.1016/j.jag.2015.06.011.

633 Chang, B., Kruger, U., Kustra, R., Zhang, J. (2013); Canonical correlation analysis
634 based on Hilbert-Schmidt independence criterion and centered kernel target alignment.
635 Proceedings of The 30th International Conference on Machine Learning, 2, 28, 316-324,
636 http://jmlr.csail.mit.edu/proceedings/papers/v28/chang13.pdf.

637 Chen, J.L., Wilson, C.R., Famiglietti, J.S., Rodell, M., (2007); Attenuation effect on

638 seasonal basin-scale water storage changes from GRACE time-variable gravity. Journal
639 of Geodesy, 81, 4, 237-245, doi:10.1007/s00190-006-0104-2.

640 Chen, J. L., Wilson, C. R., Tapley, B. D., Yang, Z. L., Niu, G. Y. (2009); 2005 drought
641 event in the Amazon River basin as measured by GRACE and estimated by climate
642 models. J. Geophys. Res., 114, B05404, doi:10.1029/2008JB006056.

643 Dee, D. P., et al. (2011); The ERA-Interim reanalysis: configuration and performance of
644 the data assimilation system. Q. J. R. Meteorol. Soc., 137, 553-597, doi:10.1002/qj.828.

645 Döll, P., Kaspar, F., Lehner, B. (2003); A global hydrological model for deriving wa-
646 ter availability indicators: model tuning and validation. J. Hydrol., 270, 105-134,
647 doi:10.1016/S0022-1694(02)00283-4.

648 Edwards, D.C., McKee, T.B. (1997); Characteristics of 20th century drought in the
649 United States at multiple time scales. Climatology Report No. 97-2, Colorado State
650 Univ., Ft. Collins, CO.

651 Eicker, A., Forootan, E., Springer, A., Longuevergne, L., Kusche, J. (2016); Does
652 GRACE see the terrestrial water cycle 'intensifying'? Journal of Geophysical Research-
653 Atmosphere, 121, 733-745, doi:10.1002/2015JD023808.

654 Feng, H., Zhang, M. (2015); Global land moisture trends: drier in dry and wetter in wet
655 over land. Scientific Reports, 5, doi:10.1038/srep18018.

656 Ferreira, V.G., Asiah, Z., Xu, J., Gong, Z., Andam-Akorful, S.A. (2018); Land water-
657 storage variability over West Africa: inferences from space-borne sensors. Water, 10,
658 380-405, doi:10.3390/w10040380.

659 Folger, F., Cody, B.A. (2015); Drought in the United States: causes and current under-
660 standing. Congressional Research Service, 7-5700, www.crs.gov, R43407

661 Foresta, L., Gourmelen, N., Weissgerber, F., Nienow, P., Williams, J.J., Shepherd, A.,
662 Drinkwater, M.R., Plummer, S. (2018); Heterogeneous and rapid ice loss over the

663 Patagonian ice fields revealed by CryoSat-2 swath radar altimetry. Remote Sensing of
664 Environment, 211, 441-455, doi:10.1016/j.rse.2018.03.041.

665 Forootan, E., Kusche, J. (2012); Separation of global time-variable gravity signals into
666 maximally independent components. J Geod, 86: 477-497, doi:10.1007/s00190-011-
667 0532-5.

668 Forootan, E., Kusche, J., Talpe, M., Shum, C.K., Schmidt, M. (2018); Developing a
669 complex independent component analysis (CICA) technique to extract non-stationary
670 patterns from geophysical time series. Surv Geophys., 39, 435-465, doi:10.1007/s10712-
671 017-9451-1.

672 Forootan, E., Safari, A., Mostafaie, A., Schumacher, M., Delavar, M., Awange, J.L.
673 (2017); Large-scale total water storage and water flux changes over the arid and semi-
674 arid parts of the Middle East from GRACE and reanalysis products. Surveys in Geo-
675 physics, 38 (3), 591-615, doi:10.1007/s10712-016-9403-1.

676 Forootan, E., Khandu, Awange, J., Schumacher, M., Anyah, R., van Dijk, A., Kusche,
677 J., (2016); Quantifying the impacts of ENSO and IOD on rain gauge and remotely
678 sensed precipitation products over Australia. Remote Sensing of Environment,172, 50-
679 66, doi:10.1016/j.rse.2015.10.027.

680 Forootan, E., Rietbroek, R., Kusche, J., Sharifi, M. A., Awange, J., Schmidt, M.,
681 Omondi, P., Famiglietti, J. (2014); Separation of large scale water storage patterns
682 over Iran using GRACE, altimetry and hydrological data. Remote Sensing of Environ-
683 ment, 140, 580-595. http://doi.org/10.1016/j.rse.2013.09.025.

684 Forootan, E., Statistical signal decomposition techniques for analyzing time-variable
685 satellite gravimetry data. PhD Thesis, University of Bonn, https://d-nb.info/
686 1060824507/34.

687 Forootan, E., Awange, J., Kusche, J., Heck, B., Eicker, A. (2012); Independent patterns
688 of water mass anomalies over Australia from satellite data and models. Remote Sensing
689 of Environment, 124, 427-443, doi:10.1016/j.rse.2012.05.023.

690 Frappart, F., Ramillien, G. (2012); Contribution of GRACE satellite gravimetry in global
691 and regional hydrology, and ice sheets mass balance. In Water Resources Management
692 and Modeling, Nayak P (ed). Intech, 191-214.

693 Garćia-Garćia, D., Ummenhofer, C.C., Zlotnicki, V. (2011); Australian water mass vari-
694 ations from GRACE data linked to Indo-Pacific climate variability. Remote Sensing of
695 Environment, 115, 2175-2183, doi:10.1016/j.rse.2011.04.007.

696 Geruo, A., Wahr, J., Zhong, J. (2013); Computations of the viscoelastic response of a 3-D
697 compressible Earth to surface loading: an application to Glacial Isostatic Adjustment
698 in Antarctica and Canada. Geophys. J. Int., 192 (2), 557-572, doi:0.1093/gji/ggs030.

699 Guttman, N.B. (1999); Accepting the standardized precipitation index: A calcula-
700 tion algorithm. J. Amer. Water Resour. Assoc., 35, 311-322, doi:10.1111/j.1752-
701 1688.1999.tb03592.x .

702 Hao, A., AghaKouchak, A. (2013); Multivariate standardized drought index:
703 a parametric multi-index model, Advances in Water Resources, 57, 12-18,
704 doi:10.1016/j.advwatres.2013.03.009.

705 Hirschi, M., Seneviratne, S., Schär, C. (2006); Seasonal variations in terrestrial wa-
706 ter storage for major midlatitude river basins. J. Hydrometeor., 7, 39-60, doi:
707 10.1175/JHM480.1.

708 Houborg, R., Rodell, M., Li, B., Reichle, R., Zaitchik, B.F. (2012); Drought in-
709 dicators based on model-assimilated Gravity Recovery and Climate Experiment
710 (GRACE) terrestrial water storage observations. Water Resour. Res., 48, W07525,
711 doi:10.1029/2011WR011291.

712 Humphrey, V., Gudmundsson, L, Seneviratne, S.I. (2016); Assessing global water storage
713 variability from GRACE: trends, seasonal cycle, subseasonal anomalies and extremes.
714 Surv Geophys, 37, 357-395, doi:10.1007/s10712-016-9367-1.

715 ICPDR (2017); The 2015 droughts in the Danube River Basin, Interna-
716 tional Commission for the Protection of the Danube River (ICPDR), 2017,
717 https://www.icpdr.org/main/resources/2015-droughts-danube-river-basin.

718 Khaki, M., Hoteit, I., Kuhn, M., Awange, J., Forootan, E., van Dijk, A.I.J.M., Schu-
719 macher, M., Pattiaratchi, C., (2017); Assessing sequential data assimilation techniques
720 for integrating GRACE data into a hydrological model, Advances in Water Resources,
721 107, 301-316, doi:10.1016/j.advwatres.2017.07.001.

722 Khaki, M., Forootan, E., Kuhn, M., Awange, J., Longuevergne, L., Wada, W. (2018a);
723 Efficient basin scale filtering of GRACE satellite products. Remote Sensing of Envi-
724 ronment, 204, 76-93, doi:10.1016/j.rse.2017.10.040.

725 Khaki, M., Forootan, E., Kuhn, M., van Dijk, A.I.J.M., Schumacher, M., Sharifi, M.A.
726 (2018b); Determining water storage depletion within Iran by assimilating GRACE
727 data into the W3RA hydrological model. Advances in Water Resources, 114, 1-18,
728 doi:10.1016/j.advwatres.2018.02.008.

729 Khandu, Forootan, E., Schumacher, M., Awange, J. L., Müller Schmied, H. (2016); Ex-
730 ploring the influence of precipitation extremes and human water use on total water
731 storage (TWS) changes in the Ganges-Brahmaputra-Meghna River Basin. Water Re-
732 sour. Res., 52, 2240-2258, doi:10.1002/2015WR018113.

733 Koch, K.R. (1988); Parameter estimation and hypothesis testing in linear models. New
734 York: Springer (ISBN: 978354065257).

735 Koster, R., Suarez, M.J., Heiser, M. (2000); Variance and predictability of precipitation
736 at seasonal-to-interannual timescales. J. Hydrometeor., 1, 26-46, doi:10.1175/1525-
737 7541(2000)001¡0026:VAPOPA¿2.0.CO;2.

738 Kusche, J., Eicker, A., Forootan, E., Springer, A., Longuevergne, L. (2016); Mapping
739 probabilities of extreme continental water storage changes from space gravimetry. Geo-
740 physical Research Letters, 43, 8026-8034, doi:10.1002/2016GL069538.

741 Kusche, J., Schmidt R., Petrovic, S., Rietbroek, R. (2009); Decorrelated GRACE time-
742 variable gravity solutions by GFZ and their validation using a hydrological model.
743 Journal of Geodesy, 83 (10), 903-913, doi:10.1007/s00190-009-0308-3.

744 Leblanc, M. J., Tregoning, P., Ramillien, G., Tweed, S.O., Fakes, A. (2009); Basin-
745 scale, integrated observations of the early 21st century multiyear drought in southeast
746 Australia. Water Resour. Res., 45, W04408, doi:10.1029/2008WR007333.

747 L'Heureux, M.L., Tippett, M.K., Barnston, A.G. (2015); Characterizing ENSO coupled
748 variability and its impact on North American seasonal precipitation and temperature.
749 J. Climate, 28, 4231-4245, doi:10.1175/JCLI-D-14-00508.1.

750 Li, B., Rodell, M., Zaitchik, B.F., Reichle, R.H., Koster, R.D., van Dam, T.M. (2012);
751 Assimilation of GRACE terrestrial water storage into a land surface model: evaluation
752 and potential value for drought monitoring in western and central Europe. Journal of
753 Hydrology, 446-447, 103-115, doi:10.1016/j.jhydrol.2012.04.035.

754 Long, D., Scanlon, B. R., Longuevergne, L., Sun, A.-Y., Fernando, D. N., Save, H.
755 (2013); GRACE satellites monitor large depletion in water storage in response to the
756 2011 drought in Texas, Geophys. Res. Lett., 40, 3395-3401, doi:10.1002/grl.50655.

757 McKee, T.B., Doesken, N.J., Kleist, J. (1993); The relationship of drought frequency
758 and duration of time scales. Eighth Conference on Applied Climatology, American
759 Meteorological Society, Jan17-23, 1993, Anaheim CA, pp.179-186.

760 Mishra, A.K., Singh, V.P. (2010); A review of drought concepts. Journal of Hydrology,
761 391, 202-216, doi:10.1016/j.jhydrol.2010.07.012.

762 Mpelasoka, F., Awange, J.L., Zerihun, A. (2017); Influence of coupled ocean-atmosphere
763 phenomena on the Greater Horn of Africa droughts and their implications. Science of
764 The Total Environment, 610-611, 691-702, doi:10.1016/j.scitotenv.2017.08.109.

765 Mueller, B. (2012); Evapotranspiration and terrestrial water storage in the global climate
766 system. ETH, doi:10.3929/ethz-a-7356967.

767 Müller Schmied, H., Eisner, S., Franz, D., Wattenbach, M., Portmann, F., Flörke, M.,
768 Döll, P. (2014); Sensitivity of simulated global-scale freshwater fluxes and storages to
769 input data, hydrological model structure, human water use and calibration, Hydrol.
770 Earth. Syst. Sci., 18, 3511-3538, doi:10.5194/hess-18-3511-2014.

771 Narasimhan, B., Srinivasan, R., (2005); Development and evaluation of Soil
772 Moisture Deficit Index (SMDI) and Evapotranspiration Deficit Index (ETDI)
773 for agricultural drought monitoring. Agri. Forest Meteorol. 133(1-4), 69-88,
774 doi:10.1016/j.agrformet.2005.07.012 .

775 Ni, S., Chen, J., Wilson, C.R., Li, J., Hu, X., Fu, R. (2018); Global terrestrial
776 water storage changes and connections to ENSO events. Surv Geophys., 39, 1-12,
777 doi:10.1007/s10712-017-9421-7.

778 Omondi, P.A., Awange, J.L., Forootan, E., Ogallo, L.A., Barakiza, R., Girmaw, G.B.,
779 Fesseha, I., Kululetera, V., Kilembe, C., Mbati, M.M., Kilavi, M., King'uyu, S.M.,
780 Omeny, P.A., Njogu, A., Badr, E. M., Musa, T. A., Muchiri, P., Bamanya, D., Komu-
781 tunga, E. (2014); Changes in temperature and precipitation extremes over the Greater
782 Horn of Africa region from 1961 to 2010. International Journal of Climatology, 34,
783 1262-1277, doi:10.1002/joc.3763.

784 Phillips, T., Nerem, R. S., Fox-Kemper, B., Famiglietti, J. S., Rajagopalan, B. (2012);
785 The influence of ENSO on global terrestrial water storage using GRACE. Geophysical
786 Research Letters, 39, L16705, doi:10.1029/2012GL052495.

787 Rajsekhar, D., Singh, V.P., Mishra, A.K. (2015); Multivariate drought index: An infor-
788 mation theory based approach for integrated drought assessment. Journal of Hydrology,
789 526, 164-182, doi:10.1016/j.jhydrol.2014.11.031.

790 Rakovec, O., Kumar, R., Mai, J., Cuntz, M., Thober, S., Zink, M., Attinger, S.,
791 Schäfer, D., Schrön, M., Samaniego, L. (2016); Multiscale and multivariate evaluation
792 of water fluxes and states over European river basins. J. Hydrometeor., 17, 287-307,
793 doi:10.1175/JHM-D-15-0054.1 .

794 Ramillien, G., Frappart, F., Cazenave, A., Güntner, A. (2005). Time variations of land
795 water storage from an inversion of 2 years of GRACE geoids. Earth and Planetary
796 Science Letters, 235 (12), 283-301, doi:10.1016/j.epsl.2005.04.005.

797 Rao, S. A., Behara, S. K., Masumoto, Y., Yamagata, T. (2002); Interannual subsurface
798 variability in the tropical Indian Ocean with a special emphasis on the Indian Ocean
799 Dipole. Deep Sea Res., Part II, 49, 1549-1572, doi:10.1016/S0967-0645(01)00158-8.

800 Reynolds, R.W., Smith, T.M., Liu, C., Chelton, D.B., Casey, K.S., Schlax, M.G. (2007);
801 Daily high-resolution blended analyses for sea surface temperature. J. Climate, 20,
802 5473-5496, doi:10.1175/2007JCLI1824.1.

803 Rodell, M., Velicogna, I., Famiglietti, J.S. (2009); Satellite-based estimates of groundwa-
804 ter depletion in India. Nature, 460, 999-1002, doi:10.1038/nature08238.

805 Schellekens, J., Dutra, E., Martínez-de la Torre, A., Balsamo, G., van Dijk, A.I.J.M.,
806 Sperna Weiland, F., Minvielle, M., Calvet, J.-C., Decharme, B., Eisner, S., Fink, G.,
807 Flörke, M., Peßenteiner, S., van Beek, R., Polcher, J., Beck, H., Orth, R., Calton, B.,
808 Burke, S., Dorigo, W., Weedon, G. P. (2017); A global water resources ensemble of
809 hydrological models: the eartH2Observe Tier-1 dataset. Earth System Science Data, 9
810 (2), 389-413, doi:10.5194/essd-9-389-2017.

811 Samaniego, L., Thober, S., Kumar, R., Wanders, N., Rakovec, O., Pan, M, Zink, M.,
812 Sheffield, J., Wood, E. F., Marx, A. (2018); Anthropogenic warming exacerbates Euro-
813 pean soil moisture droughts. Nature Climate Change, 8, 421-426, doi:10.1038/s41558-
814 018-0138-5

815 Scanlon, B.R., Zhang, Z., Save, H., Sun, A.Y., Müller Schmied, H., van Beek,
816 L.P.H., Wiese, David N., Wada, Y., Long, D., Reedy, R.C., Longuevergne, L.,
817 Döll, O., Bierkens, M.F. P. (2018); Global models underestimate large decadal de-
818 clining and rising water storage trends relative to GRACE satellite data. PNAS,
819 doi:10.1073/pnas.1704665115.

820 Schumacher, M., Forootan, E., van Dijk, A.I.J.M., Müller Schmied, H., Crosbie, R.S.,
821 Kusche, J., Döll, P. (2018); Improving drought simulations within the Murray-
822 Darling Basin by combined calibration/assimilation of GRACE data into the Wa-
823 terGAP Global Hydrology Model. Remote Sensing of Environment, 204, 212-228,
824 doi:10.1016/j.rse.2017.10.029.

825 Seoane, L., Ramillien, G., Frappart, F., Leblanc, M. (2013); Regional GRACE-based es-
826 timates of water mass variations over Australia: validation and interpretation. Hydrol.
827 Earth Syst. Sci., 17, 4925-4939, doi:10.5194/hess-17-4925-2013.

828 Siderius, C., Gannon, K.E., Ndiyoi, M., Opere, A., Batisani, N., Olago, D., Par-
829 doe, J., Conway, D. (2018); Hydrological response and complex impact pathways
830 of the 2015/2016 El Niño in eastern and southern Africa. Earth's Future, 6, 2-22,
831 doi:10.1002/2017EF000680.

832 Sinha, D., Syed, T.H., Famiglietti, J.S., Reager, J.T., Thomas, R.C. (2017); Character-
833 izing drought in India using GRACE observations of terrestrial water storage deficit.
834 J. Hydrometeor., 18, 381-396, doi:10.1175/JHM-D-16-0047.1

835 Steiger, J.H., Browne, M.W. (1984); The comparison of interdependent correlations be-
836 tween optimal linear composites. Psychometrika, 49, 11-24, doi:10.1007/BF02294202.

837 Sun, A.Y., Scanlon, B.R., AghaKouchak, A., Zhang, Z. (2017); Using GRACE satellite
838 gravimetry for assessing large-scale hydrologic extremes. Remote Sens. 9(12), 1287,
839 doi:10.3390/rs9121287.

840 Strassberg, G., Scanlon, B.R., Rodell, M. (2007); Comparison of seasonal terrestrial water
841 storage variations from GRACE with groundwater-level measurements from the High
842 Plains Aquifer (USA). Geophys. Res. Lett., 34, L14402, doi:10.1029/2007GL030139.

843 Swenson, S., Chambers, D., Wahr, J., (2008); Estimating geocentervariations from a
844 combination of GRACE and ocean model output. Journal of Geophysical research,
845 113, B08410, doi:10.1029/2007JB005338.

846 Tallaksen, L.M., Van Lanen, H.A.J. (2004); Hydrological drought: processes and esti-
847 mation methods for streamflow and groundwater. Elsevier, Amsterdam, Netherlands,
848 594pp, ISBN-13: 978-0444517678.

849 Tapley, B.D., Bettadpur, S., Watkins, M., Reigber, C., (2004); The gravity recovery and
850 climate experiment: mission overview and early results. Geophys Res Lett 31:L09607,
851 doi:10.1029/2004GL019920.

852 Thomas, A.C., Reager, J.T., Famiglietti, J.S., Rodell, M., (2014); A GRACE-based water
853 storage deficit approach for hydrological drought characterization. Geophys. Res. Lett.,
854 41, 1537-1545, doi:10.1002/2014GL059323.

855 Tian, Y., Huffman, G.J., Adler, R.F., Tang, L., Sapiano, M., Maggioni, V., Wu, H.
856 (2013); Modeling errors in daily precipitation measurements: additive or multiplica-
857 tive? Geophys. Res. Lett., 40, 2060-2065, doi:10.1002/grl.50320.

858 Tiwari, V.M., Wahr, J., Swenson, S. (2009); Dwindling groundwater resources in
859 northern India, from satellite gravity observations. Geophys. Res. Lett., 36, L18401,
860 doi:10.1029/2009GL039401.

861 Trigo, R.M., Gouveia, C.M., Barriopedro, D. (2010); The intense 2007-2009 drought
862 in the Fertile Crescent: impacts and associated atmospheric circulation. Agric For
863 Meteorol, 150, 1245-1257, doi:10.1016/j.agrformet.2010.05.006.

864 van Dijk, A.I.J.M. (2010); The Australian Water Resources Assessment System: Techni-
865 cal Report 3 Landscape model (version 0.5). Technical Description. Water for a Healthy
866 Country National Research Flagship.

867 van Dijk, A.I.J.M., Renzullo, L.J., Wada, Y., Tregoning, P., (2014); A global water
868 cycle reanalysis (20032012) merging satellite gravimetry and altimetry observations
869 with a hydrological multi-model ensemble. Hydrol. Earth Syst. Sci. 18, 29552973,
870 doi:10.5194/hess-18-2955-2014.

871 van Dijk, A.I.J.M., Beck, H. E., Crosbie, R. S., de Jeu, R. A. M., Liu, Y. Y., Podger,
872 G. M., Timbal, B., Viney, N. R. (2013), The millennium drought in southeast Aus-

873 tralia (2001-2009): natural and human causes and implications for water resources,
874 ecosystems, economy, and society. Water Resour. Res., 49, doi:10.1002/wrcr.20123.

875 Van Loon, A. F. (2015); Hydrological drought explained. WIREs Water, 2: 359-392. doi:
876 10.1002/wat2.1085

877 Van Loon, A.F., Laaha, G. (2015); Hydrological drought severity explained
878 by climate and catchment characteristics, Journal of Hydrology, 526, 3-14,
879 doi:10.1016/j.jhydrol.2014.10.059.

880 Vicente-Serrano, S., Beguería, S., López-Moreno, J. (2010); A multiscalar drought index
881 sensitive to global warming: the standardized precipitation evapotranspiration index.
882 J. Climate, 23, 1696-1718, doi:10.1175/2009JCLI2909.1.

883 Voss, K.A., Famiglietti, J.S., Lo, M., Linage, C., Rodell, M., Swenson, S.C. (2013);
884 Groundwater depletion in the Middle East from GRACE with implications for trans-
885 boundary water management in the Tigris Euphrates-Western Iran region. Water Re-
886 sour Res, 49, 904-914, doi:10.1002/wrcr.20078.

887 Wahr, J., Molenaar, M., Bryan, F. (1998); Time variability of the Earth's gravity field'
888 Hydrological and oceanic effects and their possible detection using GRACE. Journal
889 of Geophysical research, 103, B12, 30, 205-229, doi:10.1029/98JB02844.

890 Wilhite, D.A. (2000); Drought: a global assessment, Routledge, London, UK.

891 Worley, S.J., Woodruff, S.D., Reynolds, R.W., Lubker, S.J., Lott, N. (2005); ICOADS
892 Release 2.1 data and products. International Journal of Climatology (CLIMAR-II Spe-
893 cial Issue), 25, 823-842, doi:10.1002/joc.1166.

894 Wu, H., Hayes, M.J., Weiss, A., Hu, Q. (2001); An evaluation of the standardized pre-
895 cipitation index, the China-z index and the statistical z-score. International Journal of
896 Climatology, 21, 745-758, doi:10.1002/joc.658.

897 Yan, H., Moradkhani, H., Zarekarizi, M. (2017); A probabilistic drought forecasting
898 framework: a combined dynamical and statistical approach. Journal of Hydrology,
899 548, 291-304, doi:10.1016/j.jhydrol.2017.03.004.

900 Yirdaw, S.Z., Snelgrove, K.R., Agboma, C.O. (2008); GRACE satellite observations
901 of terrestrial moisture changes for drought characterization in the Canadian Prairie.
902 Journal of Hydrology, 356 (1-2), 84-92, doi:10.1016/j.jhydrol.2008.04.004.

903 Zeng, N. (1999); Seasonal cycle and interannual variability in the Amazon hydrologic
904 cycle. J. Geophys. Res., 104, D8, 9097-9106, doi:10.1029/1998JD200088.

905 Zhang, D., Zhang, Q., Werner, A.D., Xiaomang, L. (2016). GRACE-based hydrological
906 drought evaluation of the Yangtze River Basin, China. J. Hydrometeor., 17, 811-828,
907 doi:10.1175/JHM-D-15-0084.1

908 Zhao, Q., Wu, W., Wu, Y. (2015); Variations in China's terrestrial water storage over
909 the past decade using GRACE data. Geodesy and Geodynamics, 6 (3), 187-193,
910 doi:10.1016/j.geog.2015.03.004.

911 Zhao, M., Velicogna, I., Kimball, J.S. (2017); A global gridded dataset of GRACE drought
912 severity index for 2002-14: comparison with PDSI and SPEI and a case study of the
913 Australia millennium drought. J. Hydrometeor., 18, 2117-2129, doi:10.1175/JHM-D-
914 16-0182.1

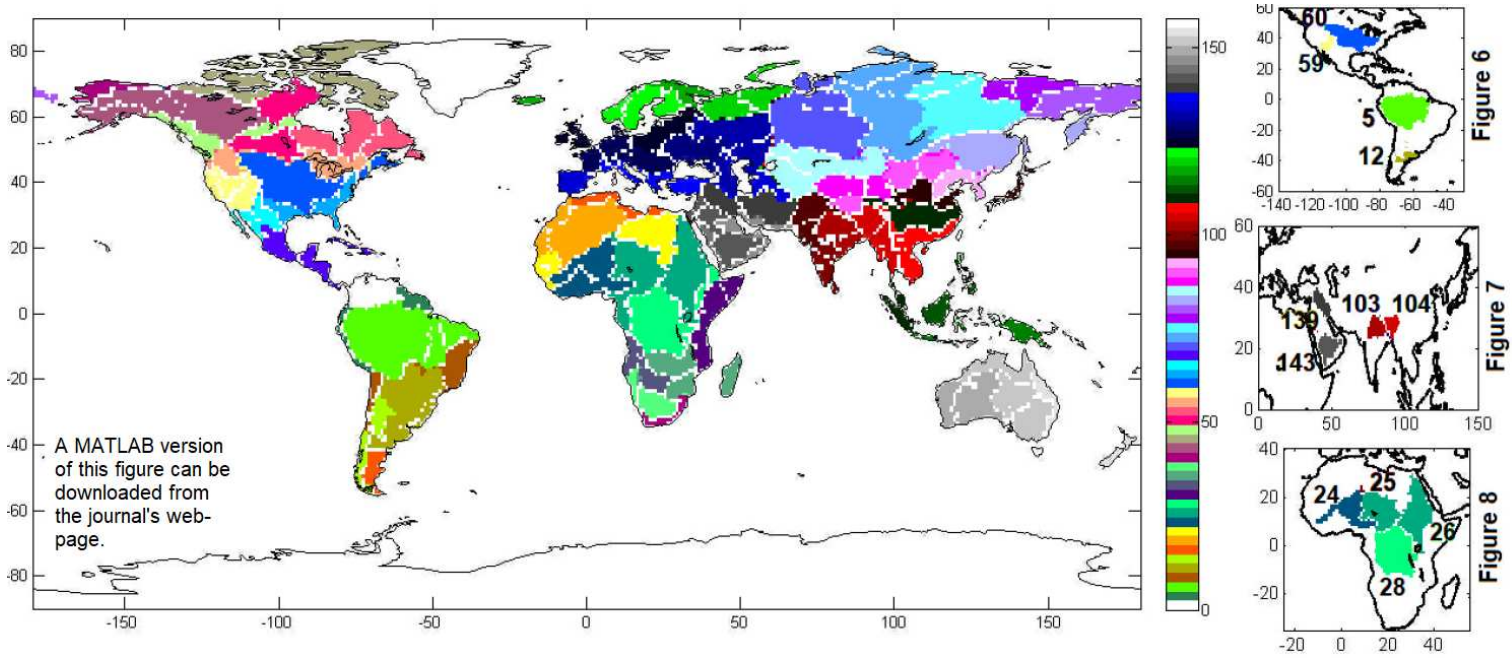

Figure 1: The world's 156 major river basins according to the Global Runoff Data Center. Identification number of each river basin is reflected in the colorbar. 1 : Magdalena + neighbor; 2 : Orinoco + coastal neighbor; 3 : Atlantic North Coast; 4 : Pacific Coast - West Amazon; 5 : Amazon; 6 : Tocantins + coasts; 7 : Paranaiba-Atlantico Nordeste; 8 : Sao Francisco-Atlantico Leste; 9 : Pacific Coast - West Parana; 10 : Parana; 11 : East Parana; 12 : Salado Atlantico; 13 : Southern Pacific Coast; 14 : Salado Pampa + Dulce; 15 : Chubut; 16 : Western Mediterranean Coast; 17 : Eastern Mediterranean Coast; 18 : North West Coast; 19 : North West Interior; 20 : North East Interior; 21 : Gambia - West Coast; 22 : Senegal; 23 : Volta - West Coast; 24 : Niger; 25 : Lake Chad - Central Interior; 26 : Nile + Red Sea neighbor; 27 : Ogooue - Central West Coast; 28 : Congo; 29 : Rift Valley; 30 : North East Coast; 31 : Jubba; 32 : Rufiji - Central East Coast; 33 : Cuanza - South West Coast; 34 : Okavango; 35 : Zambezi; 36 : Limpopo - South East Coast; 37 : Madagascar; 38 : South West Coast; 39 : Orange; 40 : South Atlantic Coast; 41 : North Yukon; 42 : Yukon; 43 : South Yukon; 44 : Mackenzie; 45 : North Mackenzie + islands; 46 : West Greenland Islands; 47 : North Fraser; 48 : Fraser and neighbors; 49 : Churchill and neighbors; 50 : Nelson; 51 : Ouest Hudson; 52 : South Hudson; 53 : Labrador - Hudson Coast; 54 : Labrador - Atlantic Coast; 55 : Saint Lawrence; 56 : Columbia; 57 : West Coast - South Columbia; 58 : Internal Basins; 59 : Colorado; 60 : Mississippi; 61 : Northern East Coast; 62 : Central East Coast; 63 : Southern East Coast; 64 : Brazos + Colorado; 65 : Rio Grande; 66 : North Western Latin America; 67 : Northern Latin America; 68 : Southern Latin America; 69 : Cuba - Saint Domingue; 70 : Ob; 71 : Taz + North and East Ob; 72 : Yenisey; 73 : Pasina + Taimyra; 74 : Chatanga; 75 : Olenek; 76 : Lena; 77 : Jana; 78 : Indigirka + neighbor; 79 : Kolyma; 80 : South Kolyma; 81 : Anadyr + Ponzina; 82 : Kamchatka; 83 : Amur; 84 : Amu and Syr Darya; 85 : Turgaj - Interior; 86 : Tes-Chem - Interior; 87 : Tarim + neighbor; 88 : Est Tarim - Interior; 89 : Tiberan plateau; 90 : Interior Loess plateau; 91 : Kerulen; 92 : Liao + Hai; 93 : Yalu; 94 : Japan; 95 : Huanghe - Yellow; 96 : Heihe + coastal neighbor; 97 : Indus; 98 : Western India; 99 : Southern India; 100 : Krishna + coastal neighbor; 101 : Godavari; 102 : Mahanadi + Neighbors; 103 : Ganges; 104 : Brahmaputra; 105 : Irrawaddy + neighbor; 106 : Salween + neighbor; 107 : Mekong + coastal; 108 : Xi + neighbor; 109 : Yangtze + coast; 110 : Malaysia; 111 : Sumatra; 112 : Borneo; 113 : Philippines; 114 : Java; 115 : Sulawesi; 116 : Papua; 117 : Iceland; 118 : Barents Sea; 119 : Northern Divina + neighbor; 120 : Pechora; 121 : Norge Sea; 122 : West Baltic Sea; 123 : East Baltic Sea; 124 : Neva + Southern Baltic Sea; 125 : Great Britain and Ireland; 126 : Loire + Seine + Garonne; 127 : Rhine + Elbe + Weser; 128 : Danube; 129 : Dniepr + Don + Dniestr; 130 : Kuban + neighbor; 131 : Volga; 132 : Ural + Northern Caspian Sea; 133 : Kura + West Caspian Sea; 134 : East Caspian Sea; 135 : Espagne; 136 : Rhone + Italie; 137 : Balkans; 138 : Turquie; 139 : Euphrates; 140 : South Caspian interior; 141 : Near East + Sinai; 142 : North interior; 143 : South interior; 144 : Red Sea - North; 145 : Red Sea - South; 146 : East Arabic; 147 : North Arabic; 148 : Coastal Iran; 149 : Ouest; 150 : Interior and South; 151 : Timor Sea; 152 : Lake Eyre; 153 : Murray; 154 : East coast; 155 : New Zealand; 156 : Tasmania.

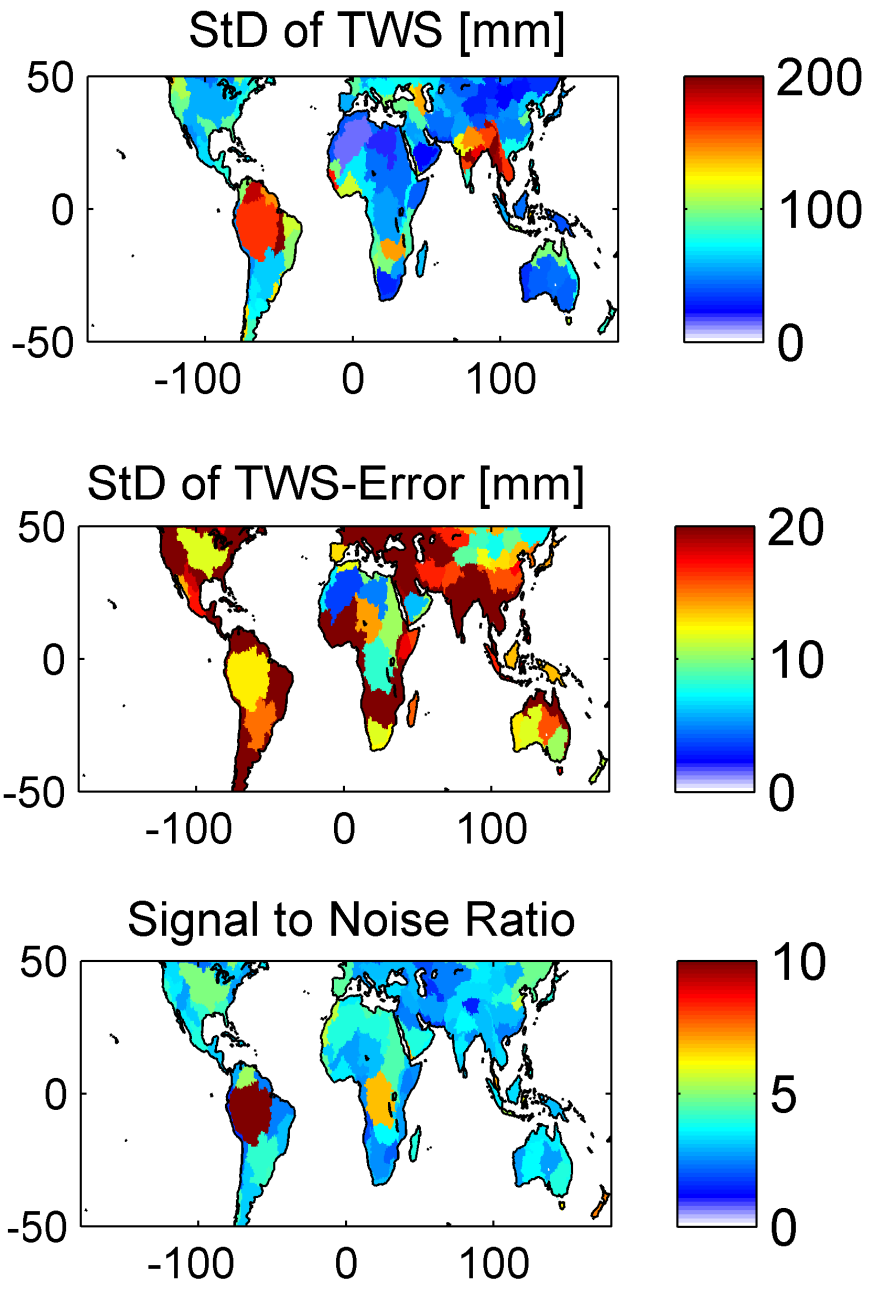

Figure 2: Overview of basin averaged GRACE TWS for 156 basins of Figure 1. (Top) Standard deviation of basin averaged GRACE TWS covering 2003–2016 showing the strength of signal. (Middle) Standard deviation of the TWS errors. (Bottom) Noise to error ration computed by dividing the top plot by the middle one.

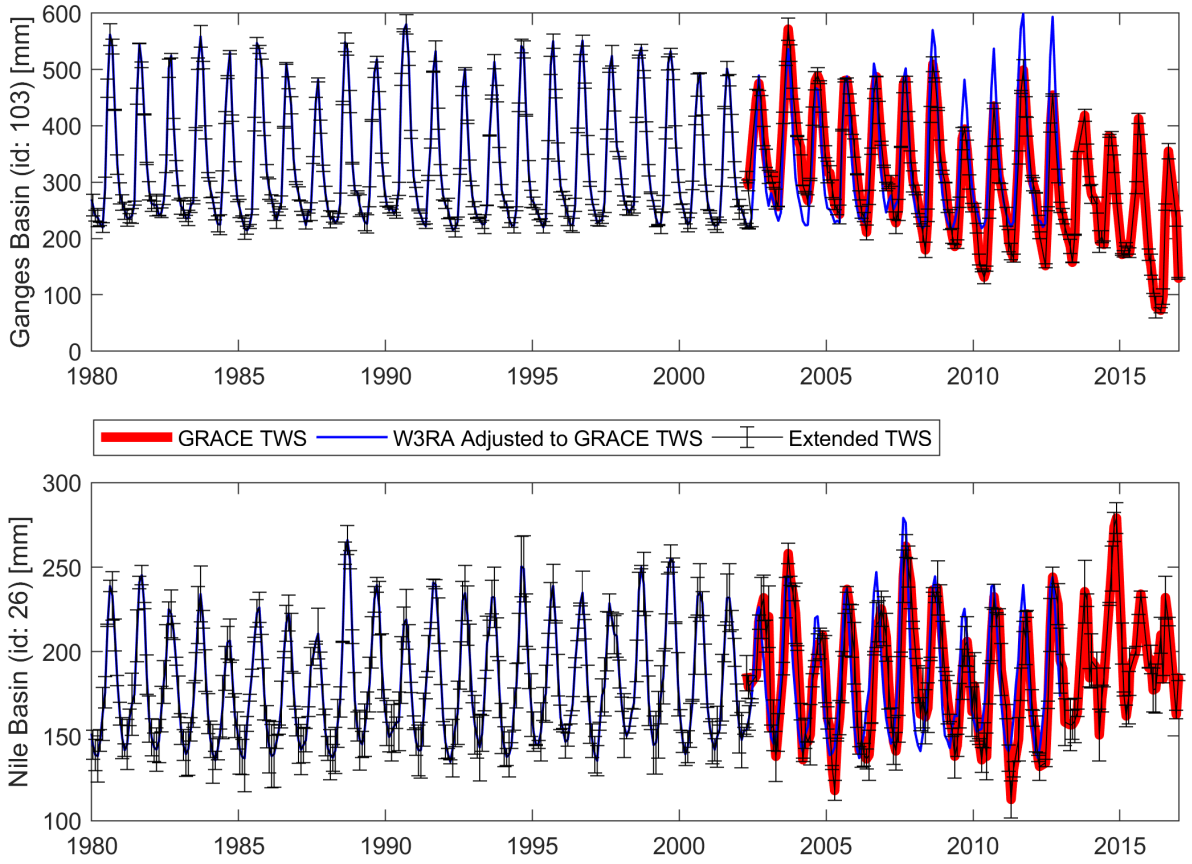

Figure 3: Time series of W3RA TWS covering 1980–2013, which is fitted to that of GRACE using the common period of 2003–2013. The extended time series of 1980–2017 are used for computing drought indices, where (top) corresponds to the Ganges River Basin, and (bottom) is related to the Nile River Basin. Errors are propagated by considering the basin average errors of Figure 2 (Middle).

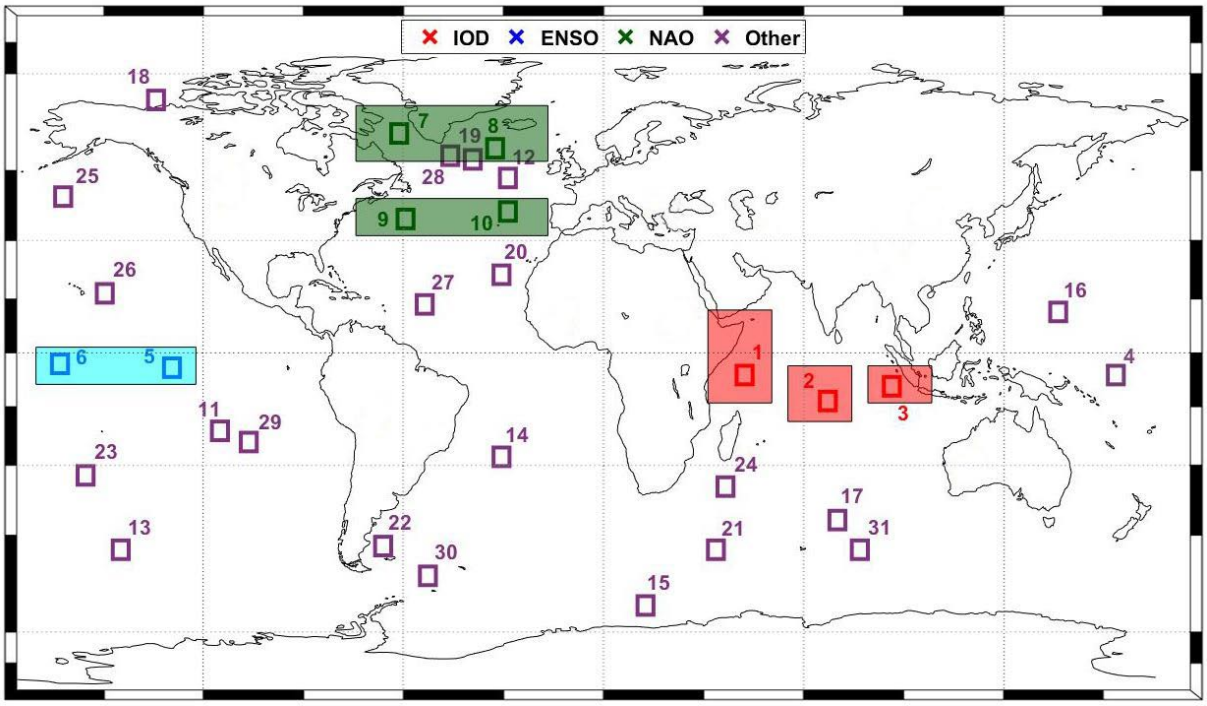

Figure 4: Locations of 5°×5° boxes, where their SST data are used to estimate CCA and relate SST records to drought indices. 10 boxes are chosen in the regions, where ENSO, IOD, and NAO are usually measured and the rest (21 boxes) are distributed to cover the global oceanic basins.

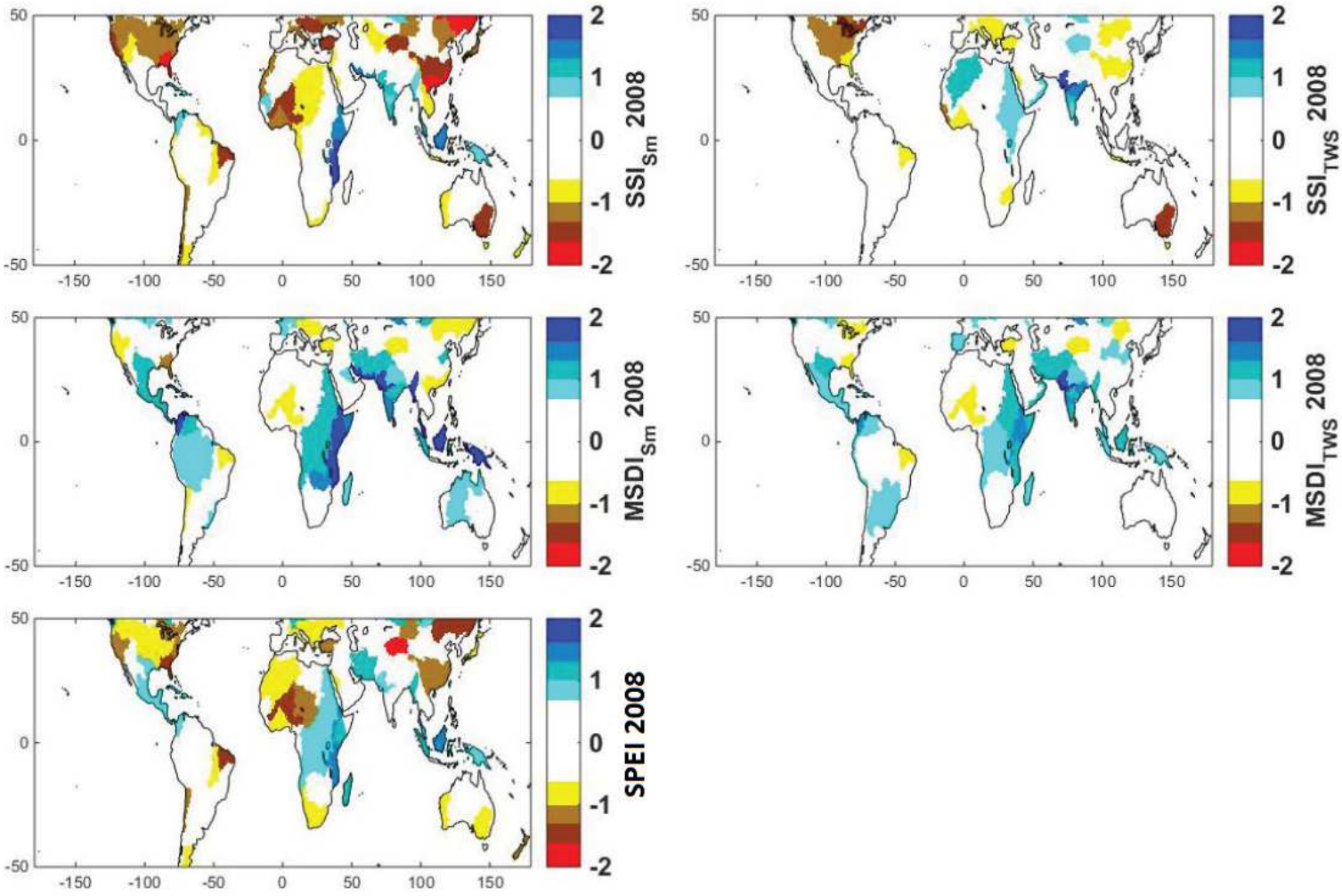

Figure 5: Global SPEI, SSI, and MSDI estimated for the 156 basins of Figure 1. The basin averaged drought indices derived for January to December 2008 are temporally averaged. Individual maps for each drought index covering 2004–2015 can be found in supplementary information.

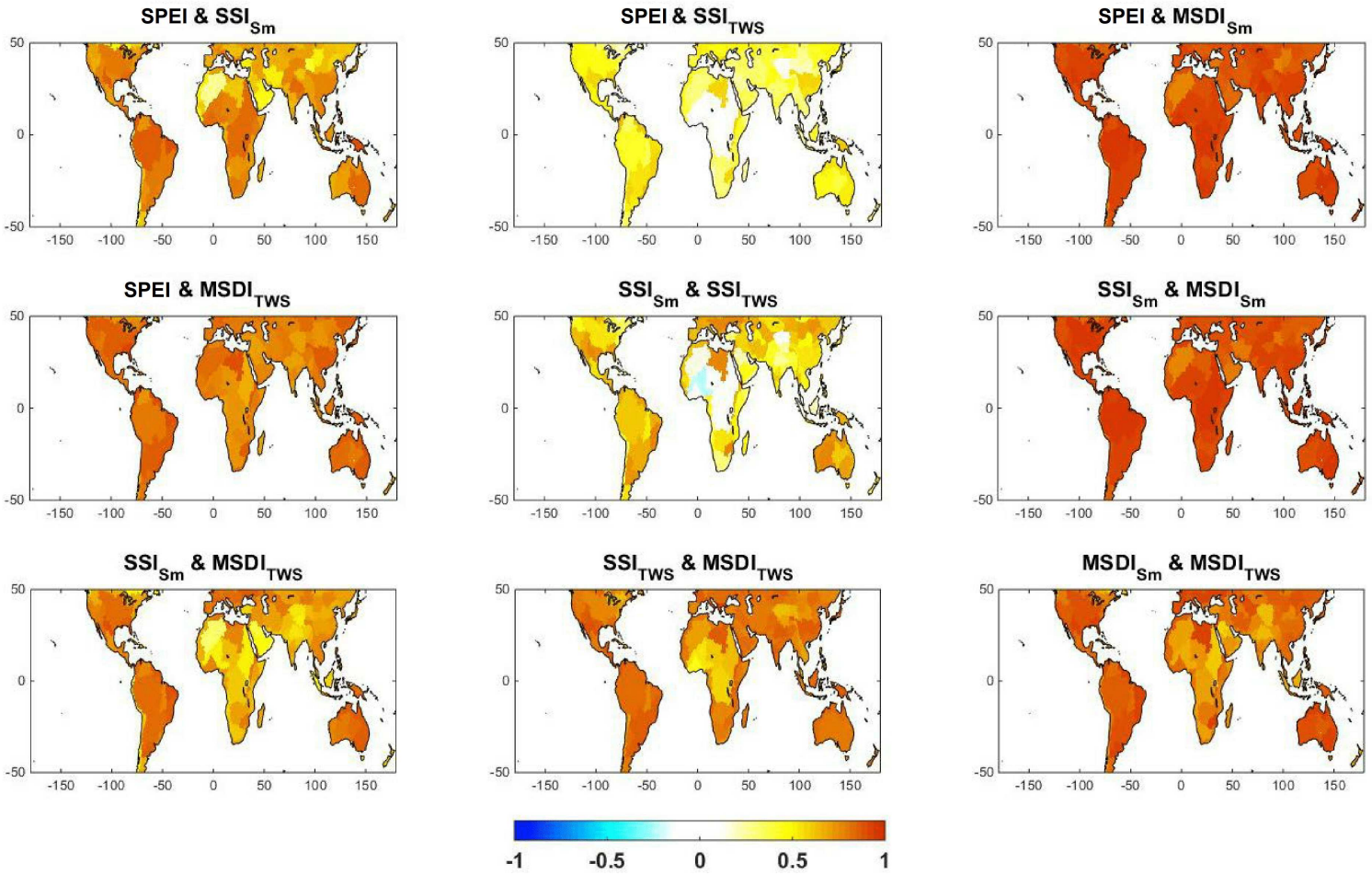

Figure 6: Correlation coefficient maps derived between drought indices over the 156 basins of Figure 1 covering 2002–2016.

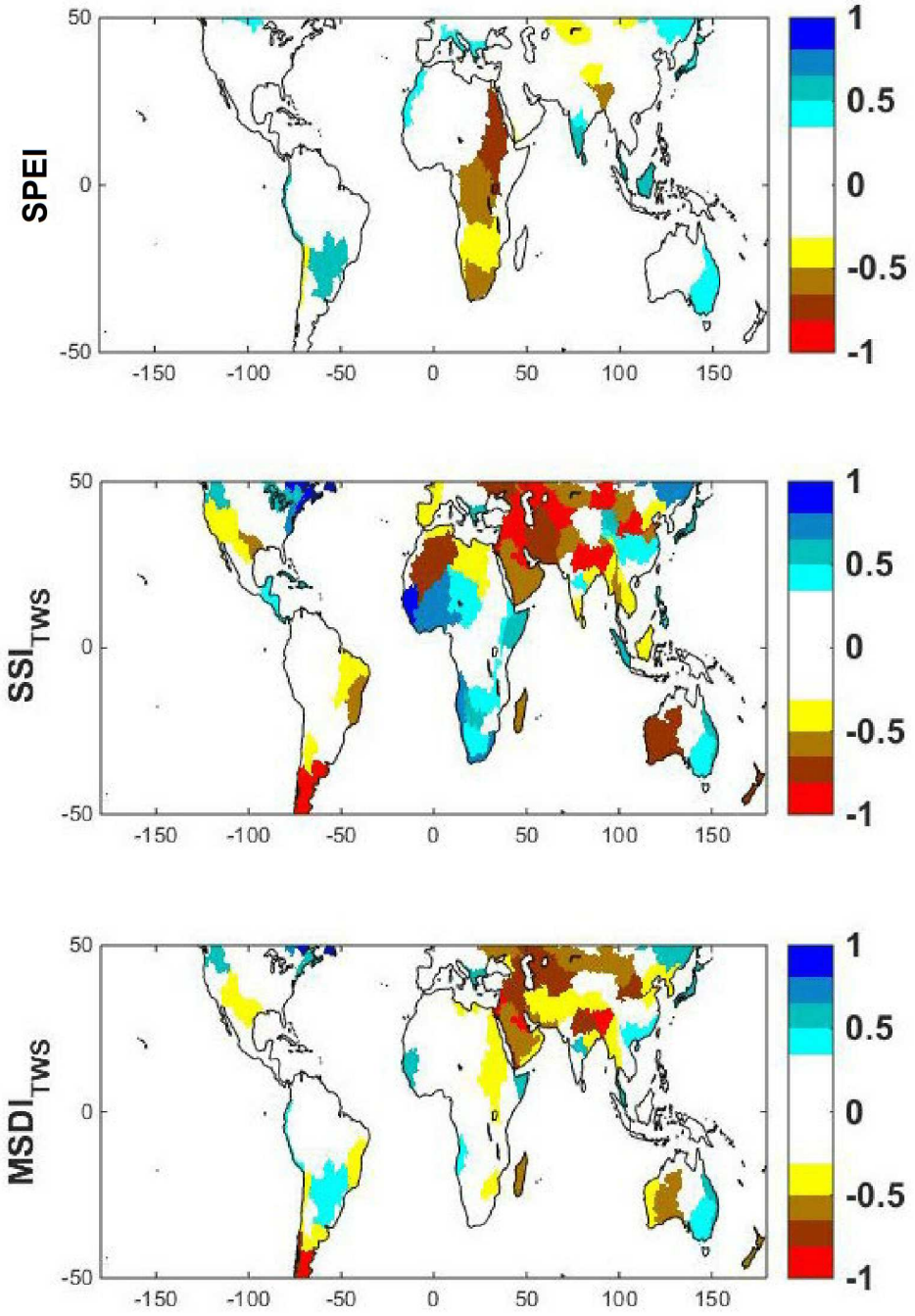

Figure 7: Average trends ([]/*year*) maps of SPEI, SSI and MSDI derived from GRACE for every basin during the study period (2002–2016).

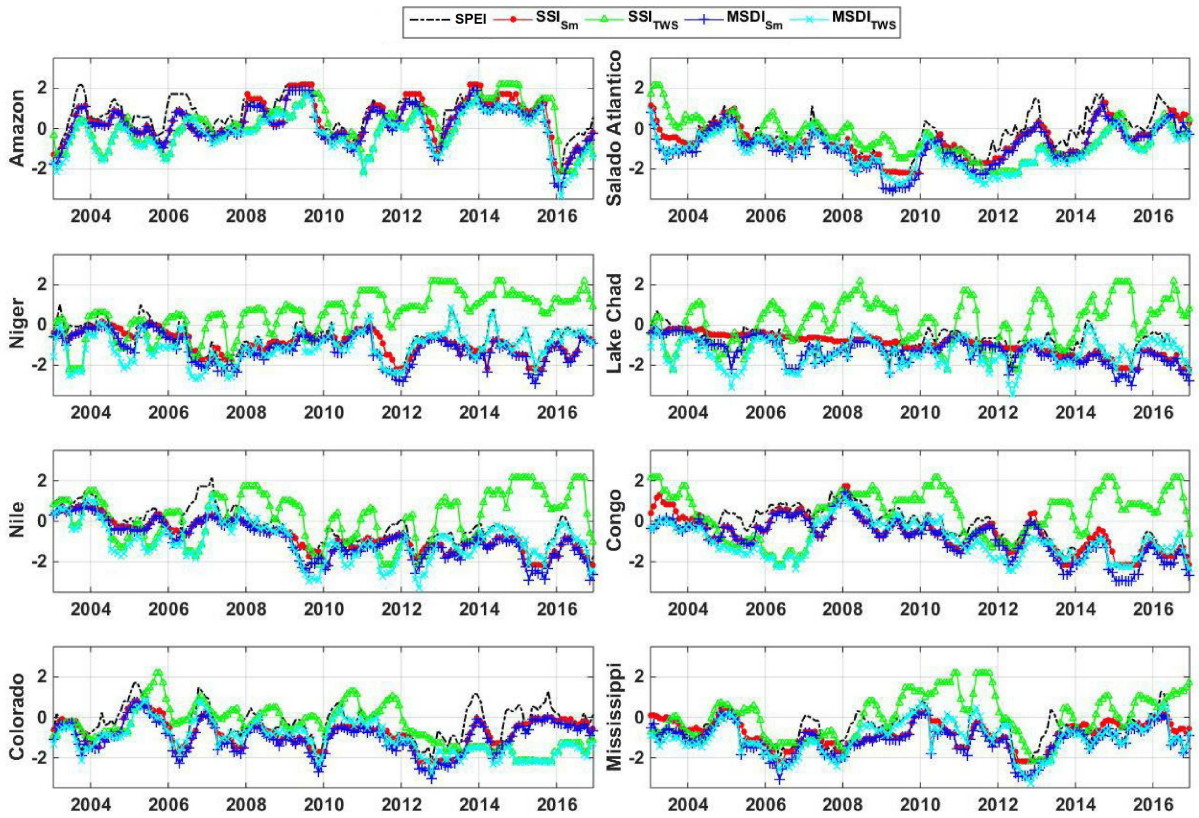

Figure 8: Drought indices computed for eight selected basins (Mississippi, Colorado, Amazon, Niger, Lake Chad, Congo, Nile, and Salado Atlantico) covering 2003–2016. Locations of the basins are shown in Figure 1. Error-bars are not shown to enhance visual comparisons. Y-axes represent the degree of dryness and wetness thus they are unit-less.

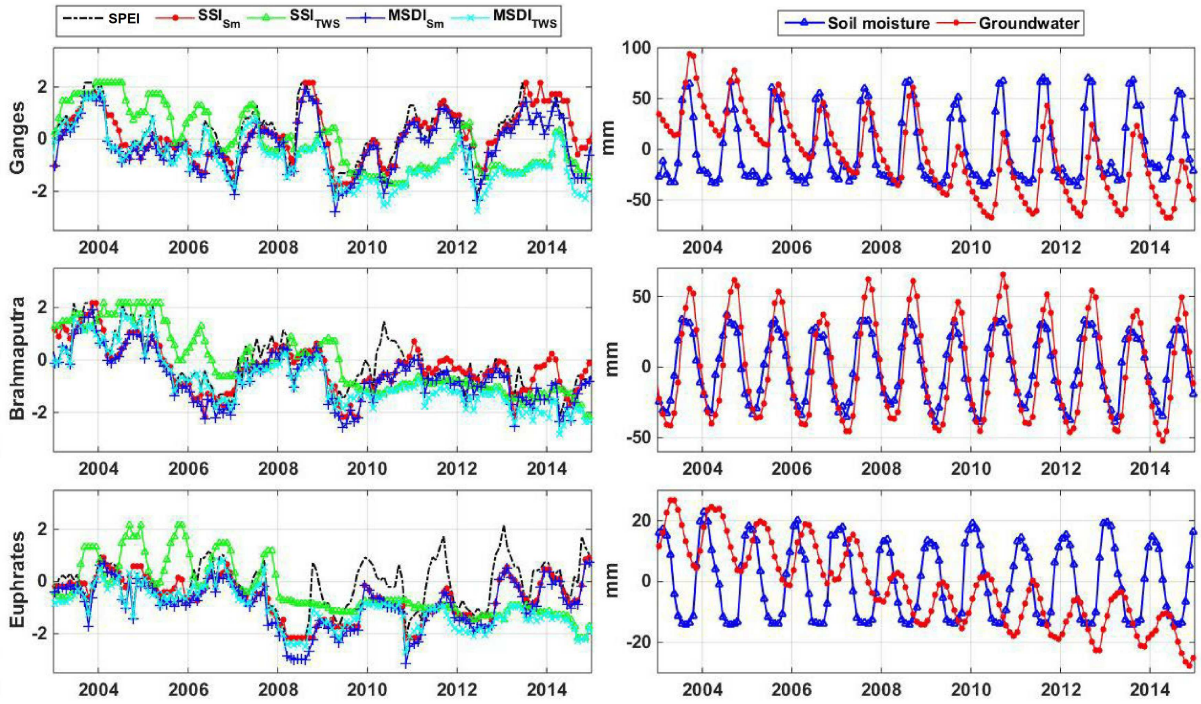

Figure 9: Drought indices computed for three selected basins within Asia (Ganges, Brahmaputra, and Euphrates) covering 2003–2016 and corresponding groundwater and soil moisture variations time series. Locations of the basins are shown in Figure 1. Error-bars are not shown to enhance visual comparisons. Y-axes of the plots on left represent the degree of dryness and wetness thus they are unit-less.

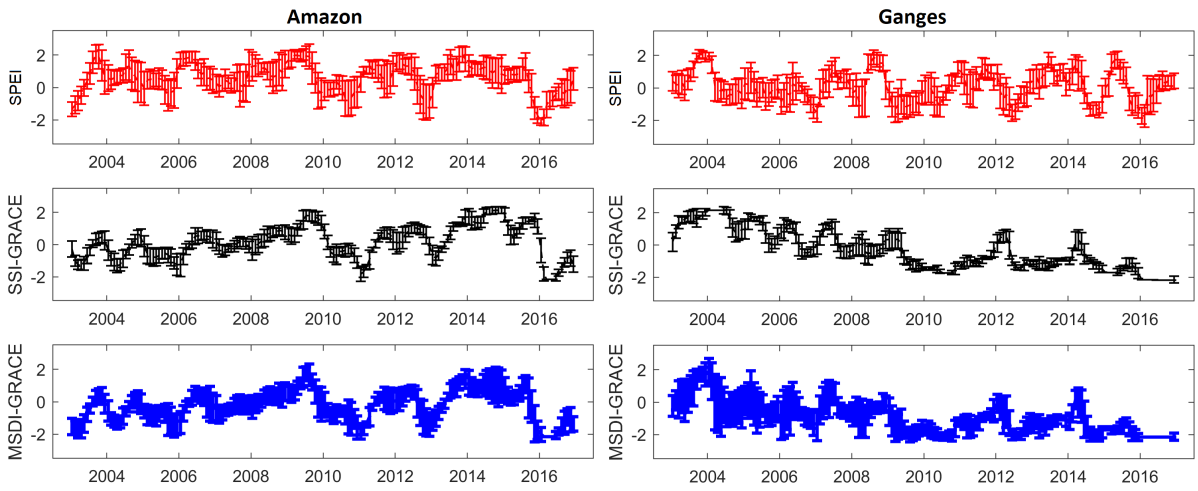

Figure 10: Drought indices and their errors computed for the Amazon (left) and Ganges (right) basins covering 2003–2016. Locations of the basins are shown in Figure 1 and y-axes represent the degree of dryness and wetness thus they are unit-less.

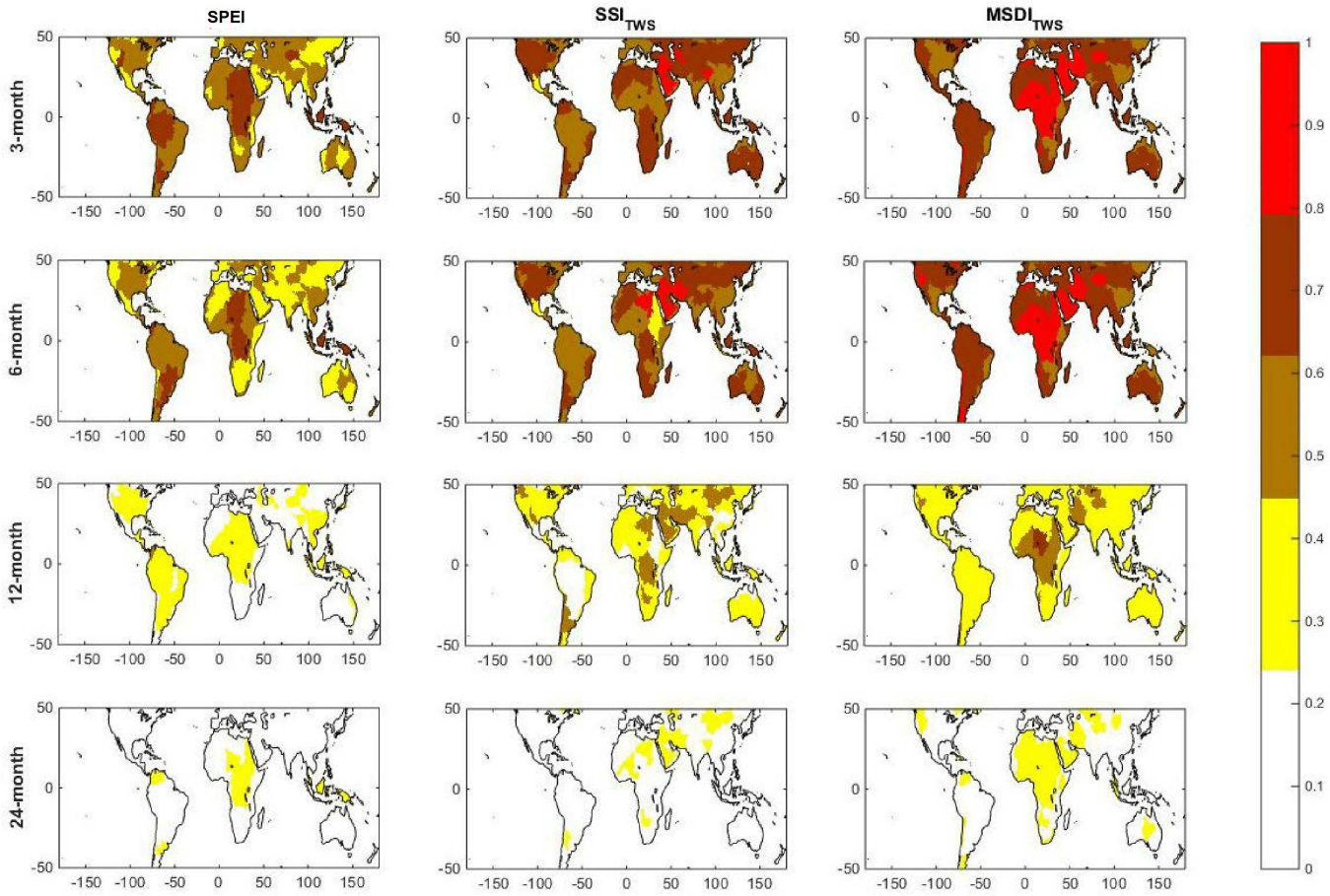

Figure 11: Basin averaged frequency (month/year) of detected droughts in different timescales for each timescale by $SPEI$, SSI, and $MSDI$.

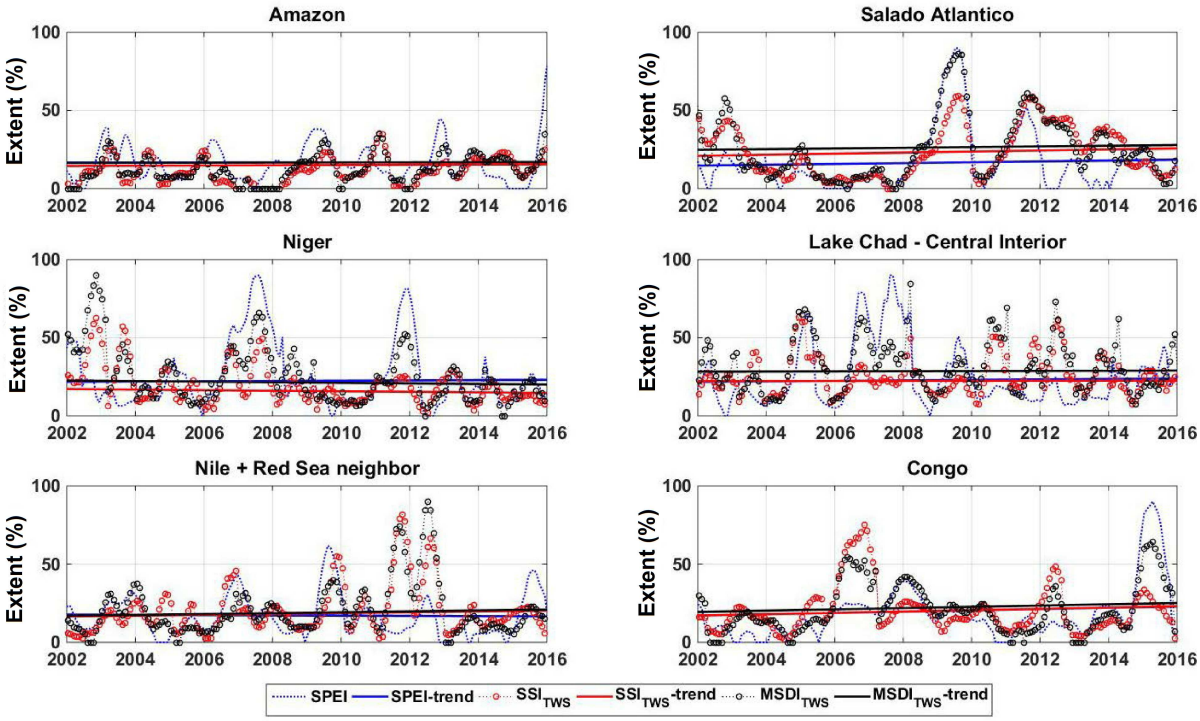

Figure 12: Time series of the areal extent of droughts within 6 arbitrary basins (Amazon, Salado Atlantico, Niger, Lake Chad - Central interior, Nile+Red Sea neighbor, and Congo). The extents are computed while considering $SPEI$, SSI, and $MSDI$ in these basins. Error-bars are not shown to enhance visual comparisons.

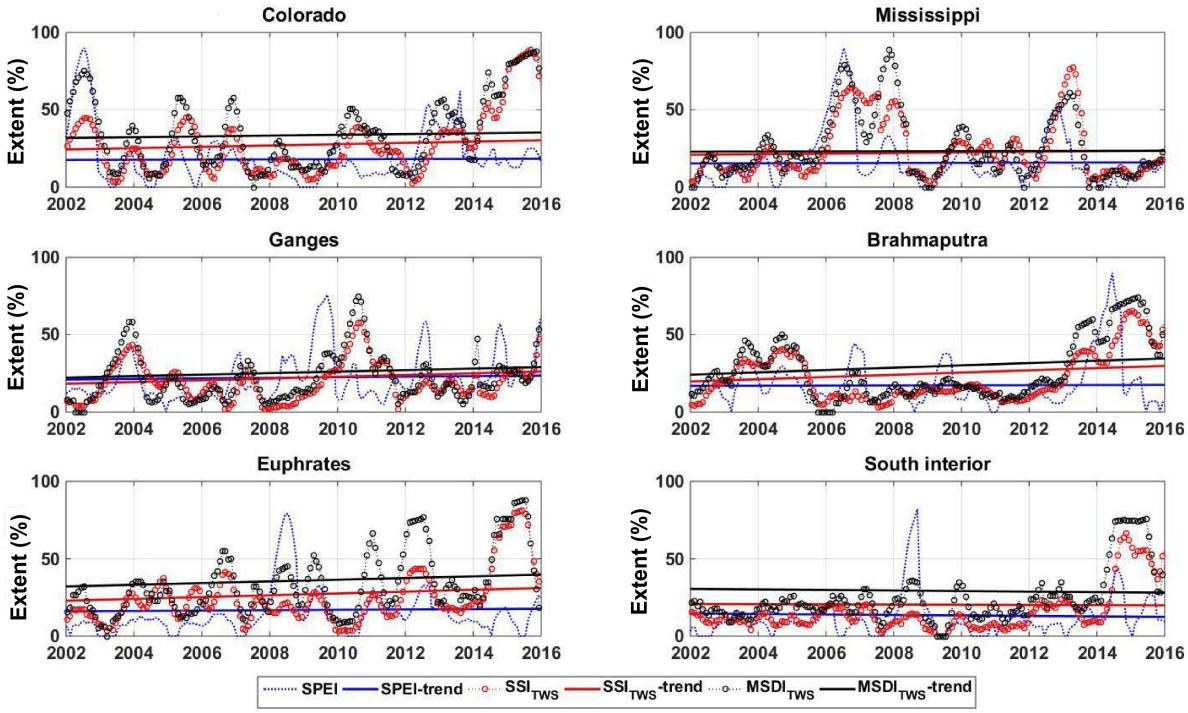

Figure 13: Similar to Figure 12 but for other 6 basins (Colorado, Mississippi, Ganges, Brahmaputra, Euphrates, and South interior). Error-bars are not shown to enhance visual comparisons.

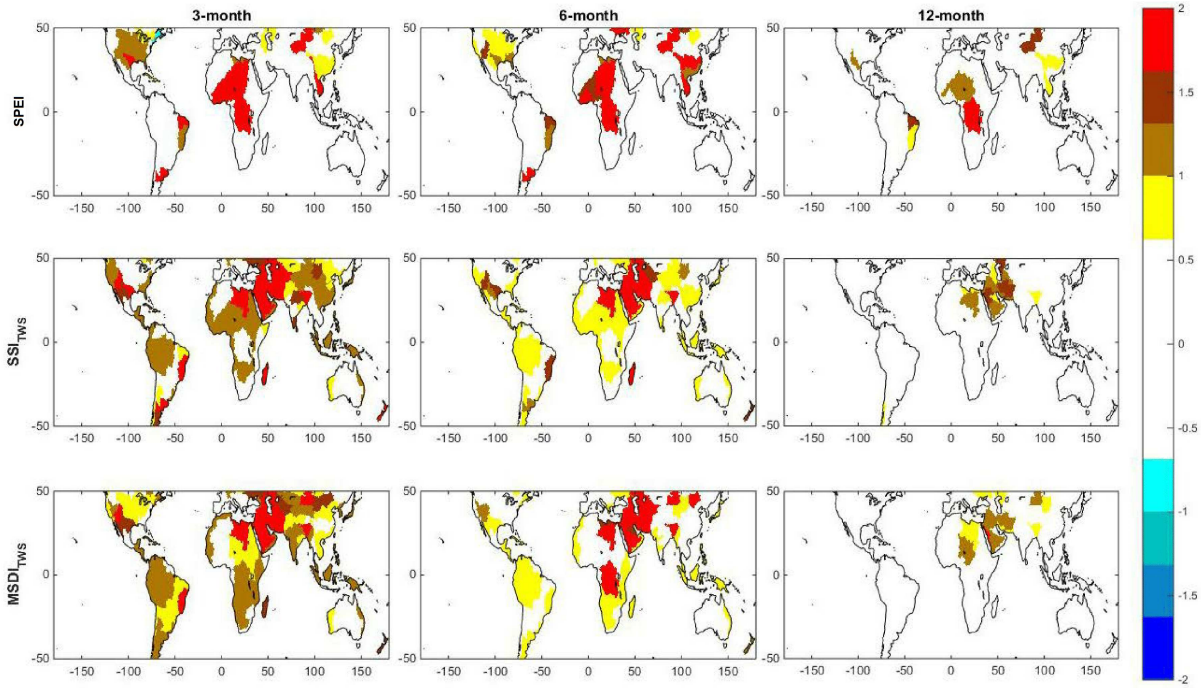

Figure 14: Areal extents of trends derived from the $SPEI$, SSI, and $MSDI$ derived for the 156 basins of Figure 1, and at different timescales. Note that no significant trend is found for the drought of 24-month time. Error-bars are not shown to enhance visual comparisons. The color-bar represents linear rate of the degree of dryness and wetness ([ ]/year).

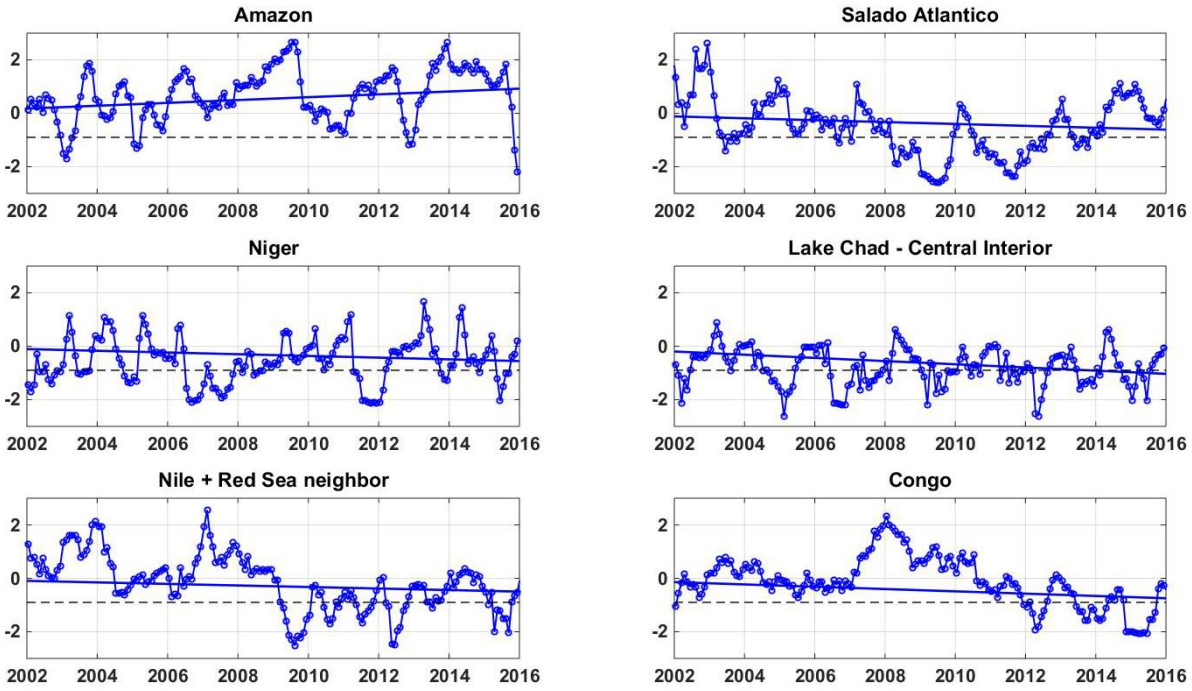

Figure 15: Extracted combinations of drought indices from the CCA, which correspond to 6 arbitrary basins (Amazon, Salado Atlantico, Niger, Lake Chad - Central interior, Nile+Red Sea neighbor, and Congo) and their linear trends. Black dashed lines represent the '-0.9' threshold value. Error-bars are not shown to enhance visual comparisons and y-axes represent the degree of dryness and wetness thus they are unit-less.

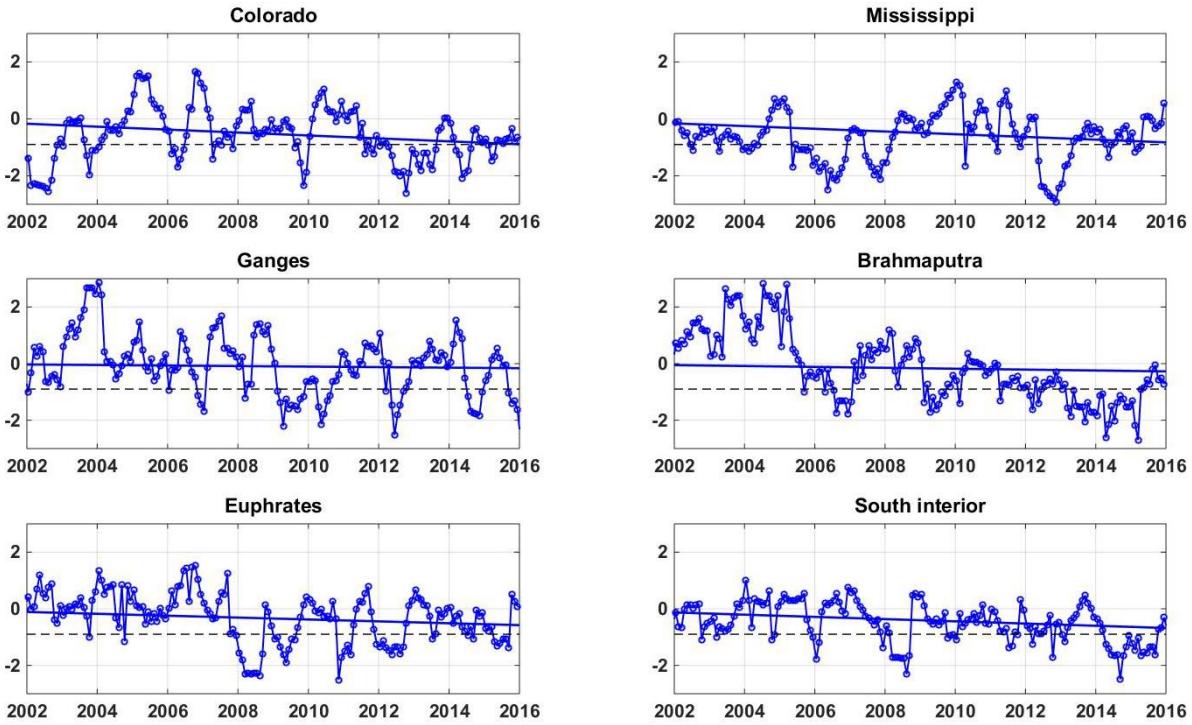

Figure 16: Similar to Figure 15 but for 6 other river basins (Colorado, Mississippi, Ganges, Brahmaputra, Euphrates, and South interior). Error-bars are not shown to enhance the visual comparisons and y-axes represent the degree of dryness and wetness thus they are unit-less.

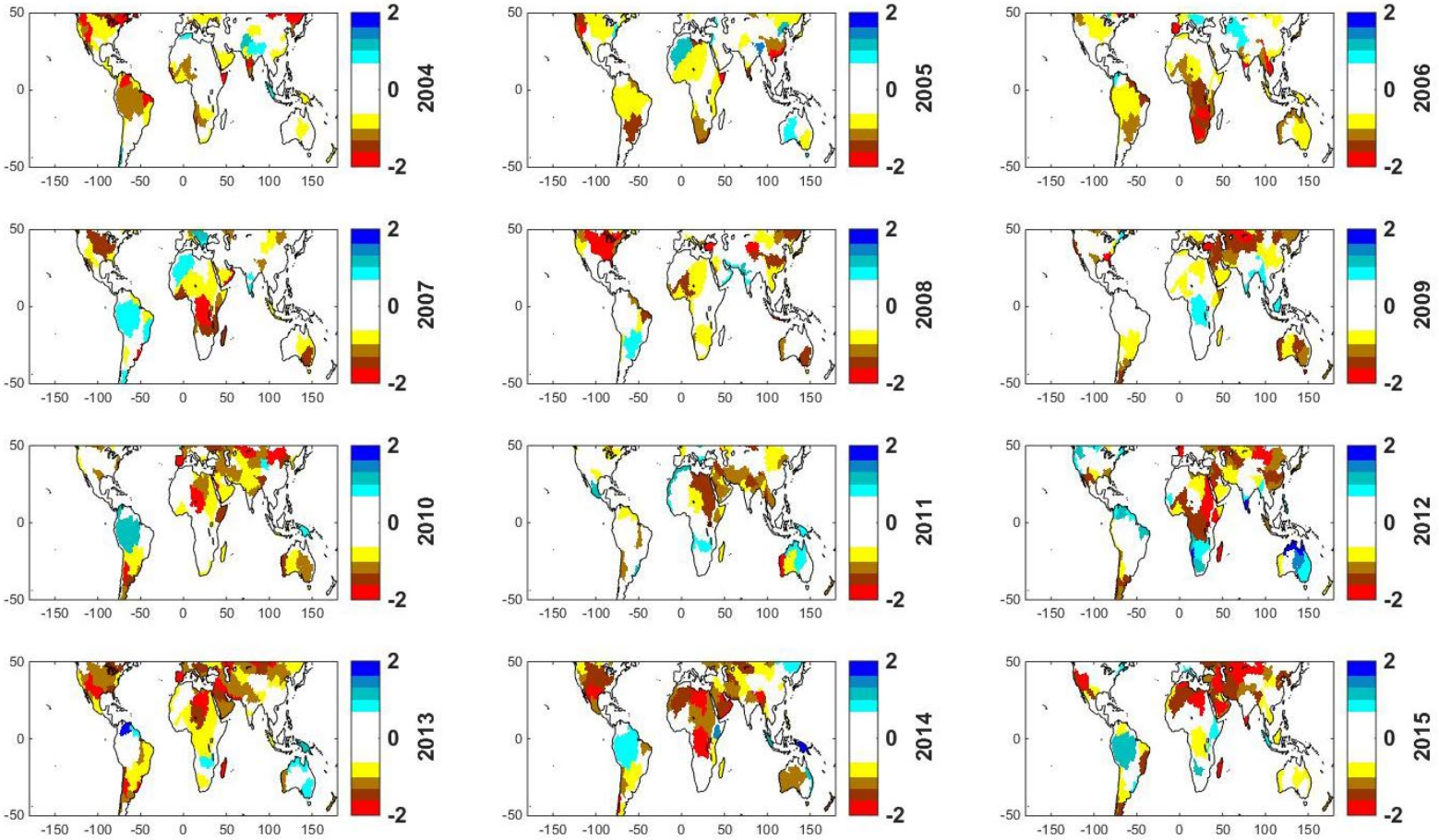

Figure 17: Detected hot spots between 2004 and 2015 based on the CCA results. Each global map indicates a combination of drought indices (SSI, $SPEI$ and $MSDI$) predicted by the CCA. The annual averages are shown here.

Table 1: A summary of the datasets used in this study.

Description	**Source**	**Acronym**	**Data access**
Terrestrial water storage	GRACE Level 2	TWS	http://www2.csr.utexas.edu/grace/
Precipitation	ERA-Interim	P	http://apps.ecmwf.int/datasets/data/interim-full-daily/
Evapotranspiration	ERA-Interim	E	http://apps.ecmwf.int/datasets/data/interim-full-daily/
Vertical summation of the total column soil moisture	ERA-Interim	Sm	http://apps.ecmwf.int/datasets/data/interim-full-daily/
Optimum Interpolation Sea Surface Temperature	AVHRR-OISST	SST	ftp://eclipse.ncdc.noaa.gov/pub/OI-daily-v2
El Niño Southern Oscillation Index	NOAA	ENSO	www.ncdc.noaa.gov/teleconnections/enso/
North Atlantic Oscillation Index	NOAA	NAO	www.ncdc.noaa.gov/teleconnections/nao/
Indian Ocean Dipole Index	NASA	IOD	http://gcmd.nasa.gov/records/GCMD_Indian_Ocean_Dipole.html

Table 2: A summary of average extent areas within the drought-affected regions for sample basins with specific drought periods.

		Areal Extent (%)		
Basin	**Drought Period**	**SPEI**	**SSI**	**MSDI**
Niger	2006–2008 (Ferreira et al., 2018)	83	51	64
Ganges	2010 (Khandu et al., 2016)	29	58	77
Brahmaputra	2005 (Khandu et al., 2016)	33	45	51
Mississippi	2012–2013 (Folger and Cody, 2015)	52	76	61
Danube	2013 (ICPDR, 2017)	71	59	86
Zambezi	2015–2016 (Siderius et al., 2018)	56	35	68

Table 3: A summary of the average and maximum correlations between estimated drought indices (using GRACE and the ERA-Interim's soil moisture data separately) and three major large-scale ocean-atmosphere interactions of ENSO, NAO, and IOD.

		NAO		**ENSO**		**IOD**	
	Drought Index	**Mean**	**Max**	**Mean**	**Max**	**Mean**	**Max**
	SPEI	0.39	0.54	0.57	0.68	0.51	0.62
By GRACE	MSDI	0.41	0.51	0.67	0.75	0.43	0.72
By GRACE	SSI	0.39	0.44	0.64	0.70	0.53	0.64
By ERA-Interim	MSDI	0.37	0.63	0.60	0.65	0.35	0.53
By ERA-Interim	SSI	0.35	0.48	0.54	0.73	0.40	0.64
	Combination	0.42	0.66	0.78	0.85	0.57	0.79